ADVANCED OPTICAL MATERIALS
www.advopticalmat.de

Phase Manipulation of Electromagnetic Waves with Metasurfaces and Its Applications in Nanophotonics

Shuqi Chen, Zhi Li, Yuebian Zhang, Hua Cheng, and Jianguo Tian*

Relative to conventional phase-modulation optical elements, metasurfaces (i.e., 2D versions of metamaterials) have shown novel optical phenomena and promising functionalities with more compact platforms and more straightforward fabrication processes. With the ability to generate a spatial phase variation, optical wavefronts can be manipulated into arbitrary shapes at will, enabling new phenomena and integrated ultrathin optical devices to be explored. This review is focused on recent developments regarding phase manipulation of electromagnetic waves with metasurfaces. Starting from their underlying physics for realizing full 2π phase manipulation, an overview of the applications of such metasurfaces in nanophotonics is discussed, concluding with a discussion of future prospects in this field.

1. Introduction

Phase is one of the basic characteristics of an electromagnetic (EM) wave. Other characteristics, such as the wave vector, polarization and amplitude, can be controlled by phase through constructive and destructive interference. According to Fermat's principle, the transition of EM waves is an accumulation effect along the propagation path. Thus, conventional optical elements used to control wavefronts require spatially varying refractive indices or geometries on their boundaries to achieve phase accumulation. However, due to the limited permittivity and permeability of natural materials, curved interfaces are typically used, which (due to their bulkiness and large weight and the need for complex design procedures) have become a barrier for the growing requirements for integration and miniaturization in modern photonic systems. Additionally, conventional optical elements are typically designed to achieve a single functionality. However, modern photonic applications require multifunctional devices, and the use of complex spatial phase variations is unpractical for phase-accumulation type optical elements. Thus, realizing phase manipulation of EM waves at the nanoscale has become a key pursuit for the development of modern optics and nanophotonics.

Metamaterials are 3D artificial nanostructures composed of periodic subwavelength unit cells that resonantly couple to the incident EM waves, exhibiting effective electric and magnetic responses not found in nature.[1–3] However, these promising potential applications are hindered in their applications due to the challenges of fabricating the required complex 3D nanostructures and the inherent metallic losses and strong dispersion of plasmonic elements at optical frequencies. Planar metamaterials, or so-called metasurfaces, can be fabricated using existing technologies, such as the lithography method and have attracted increasing attention due to their feasibility, low loss, and ease of fabrication.[4,5] The most prominent advantage of metasurfaces is that they can generate spatial phase discontinuities over the full 2π range with an optically thin interface; moreover, the resolution is less than one wavelength. Thus, wavefronts can be shaped with a distance of much less than the wavelength. With the increasing development of metasurfaces, the aforementioned limitations can be solved using various ultrathin optical devices, which have properties superior to their conventional counterparts.[6–12]

Here, we concentrate on the new capabilities of metasurfaces in recent years in manipulating the phase and propagation behaviors of EM waves. In Section 2, we briefly introduce the underlying mechanisms of three types of phase discontinuities. In Section 3, we review the basic applications of phase modulation using metasurfaces. In Section 4, we review more complex and advanced information photonics that have emerged from metasurfaces. In the last section, we provide concluding remarks and an outlook on future development directions.

2. Three Basic Types of Phase Discontinuities Generated by Metasurfaces

2.1. Resonance Phase

The pioneering approach to achieve phase discontinuities was to use the dispersion of various metallic nanoantennas, as shown in the left panel of **Figure 1**a. The optical energy is coupled to surface EM waves propagating back and forth along the antenna surface. Due to the localized surface plasmon resonance, these waves are accompanied by oscillating free electrons

Prof. S. Chen, Dr. Z. Li, Dr. Y. Zhang, Prof. H. Cheng, Prof. J. Tian
The Key Laboratory of Weak Light Nonlinear Photonics
Ministry of Education
School of Physics and Teda Applied Physics Institute
Nankai University
Tianjin 300071, China
E-mail: schen@nankai.edu.cn
Prof. S. Chen, Prof. H. Cheng, Prof. J. Tian
The Collaborative Innovation Center of Extreme Optics
Shanxi University
Taiyuan, Shanxi 030006, China
The ORCID identification number(s) for the author(s) of this article can be found under https://doi.org/10.1002/adom.201800104.

DOI: 10.1002/adom.201800104

at the surface. This process can be idealized as a simple oscillator that includes both internal and radiative damping. A charge q located at $x(t)$ with mass m on a spring with spring constant κ is driven by a harmonic incident electric field with frequency ω.[13] The charge undergoes internal damping with damping coefficient Γ_a because of the Ohmic losses

$$m\frac{\mathrm{d}^2t}{\mathrm{d}t^2}+\Gamma_\mathrm{a}\frac{\mathrm{d}x}{\mathrm{d}t}+\kappa x=qE_0\mathrm{e}^{i\omega t}+\Gamma_\mathrm{s}\frac{\mathrm{d}^3x}{\mathrm{d}t^3} \tag{1}$$

In addition to the internal damping force $\Gamma_\mathrm{a}\mathrm{d}x/\mathrm{d}t$, the charge undergoes a force $\Gamma_\mathrm{s}\mathrm{d}^3x/\mathrm{d}t^3$ due to the radiation reaction, where $\Gamma_\mathrm{s}=q^2/6\pi\varepsilon_0c^3$. This term describes the recoil exhibited by the charge as it emits radiation and is referred to as the Abraham–Lorentz force or simply the radiation reaction force.[14] By assuming harmonic motion, i.e., $x(\omega,t)=x_0\mathrm{e}^{i\omega t}$, the steady-state solution of Equation (1) can be written as

$$x(\omega,t)=\frac{(q/m)E_0}{\left(\omega_0^2-\omega^2\right)+i\frac{\omega}{m}\left(\Gamma_\mathrm{a}+\omega^2\Gamma_\mathrm{s}\right)}\mathrm{e}^{i\omega t}=x_0(\omega)\mathrm{e}^{i\omega t} \tag{2}$$

where $x_0(\omega)$ contains the amplitude and phase response of the oscillator and $\omega_0=\sqrt{k/m}$. Equation (2) implies that the amplitude of the oscillation is in phase with the incident field for $\omega\to 0$ and is phase delayed by π for $\omega\to\infty$; thus, the tuning range of the phase is up to π if a single antenna resonance is involved. Using multiresonance nanoantennas, the phase response can be extended to cover the entire 2π range, which is necessary to fully control EM waves. V-shaped optical nanoantennas that work in the midinfrared (MIR) range were the first experimentally demonstrated nanostructures to achieve a phase coverage of 2π due to the two different plasmonic eigenmodes that were supported according to their current distributions, as illustrated in Figure 1b.[4,15] The scalability of this nanostructure allows its extension to other frequency ranges, such as the near-infrared (NIR) range[5] and the visible range via Babinet-inverted nanoapertures.[16] Notably, only the cross-polarized light is engineered with an anomalous behavior with an efficiency of 10–20%, while the co-polarized counterpart propagates normally. Several approaches have been proposed to boost the efficiency, such as bilayer plasmonic metasurfaces obtained by coupling the nanoantennas with their complementary Babinet-inverted copy[17] and the introduction of a Fabry–Pérot-like cavity.[18]

To improve the manipulation efficiency, reflection arrays consisting of metallic antennas and a back metallic plane separated by a thin dielectric layer have been demonstrated.[19,20] Strong near-field coupling can be induced between the top nanoantennas and their reflections in the metallic plane due to the existence of the dielectric layer; additionally, a strong magnetic field can be confined inside the dielectric layer because of the antiparallel induced currents on the top nanoantennas and the metallic plane, known as gap-surface plasmon modes.[21,22] The essence of reflection arrays is to use top nanoantennas coupled with their dipolar reflections in the metallic plane to achieve a phase variation of 2π. Ideally, all incident light can be converted into an anomalous reflection by blocking the transmission with the metallic ground plane, which has the same polarization state as the incidence. Experiments have demonstrated that the efficiency in generating anomalous reflection of this configuration reaches 80%, significantly higher than the single-antenna strategy.

Metamaterial Huygens' surfaces have been proposed to boost the controlling efficiency in the transmission configuration by matching the impedance of metamaterials with that of free space. The reflection can be completely eliminated by tuning the surface electric and magnetic polarizabilities of the metamaterials $\bar{\bar{\alpha}}_\mathrm{e}^\mathrm{eff}$ and $\bar{\bar{\alpha}}_\mathrm{m}^\mathrm{eff}$, respectively. Then, the electric sheet admittance ($\bar{\bar{Y}}_\mathrm{es}=j\omega\bar{\bar{\alpha}}_\mathrm{e}^\mathrm{eff}$) and the magnetic sheet impedance

Shuqi Chen is a professor at the Key Laboratory of Weak Light Nonlinear Photonics, Ministry of Education, School of Physics and Teda Institute of Applied Physics, Nankai University, China. He received his joint training Ph.D. degree from the University of Arizona, USA, and Nankai University, China, in 2009. He was a winner of the New Century Excellent Talents Support Program of Ministry of Education of China in 2013. Prof. Chen's current research interests include nonlinear optics, phononics and acoustics of metasurfaces, and subwavelength electromagnetics.

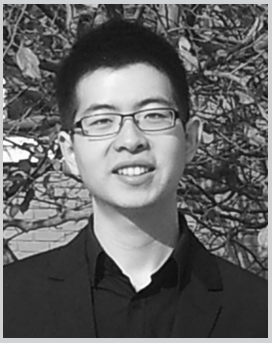

Zhi Li is a doctoral candidate student at the Key Laboratory of Weak Light Nonlinear Photonics, Ministry of Education, School of Physics and Teda Institute of Applied Physics, Nankai University, China. He received his bachelor's degree in materials physics from Nankai University in 2015. His current research focuses on nonlinear nanophotonics.

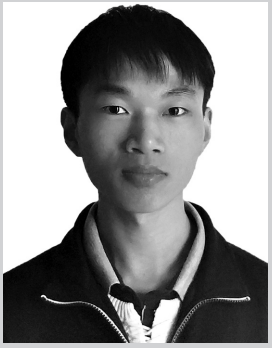

Yuebian Zhang is a doctoral candidate student at the Key Laboratory of Weak Light Nonlinear Photonics, Ministry of Education, School of Physics and Teda Institute of Applied Physics, Nankai University, China. He received his bachelor's degree in applied physics from Inner Mongolia University of Science & Technology in 2015. His current research focuses on nanophotonics.

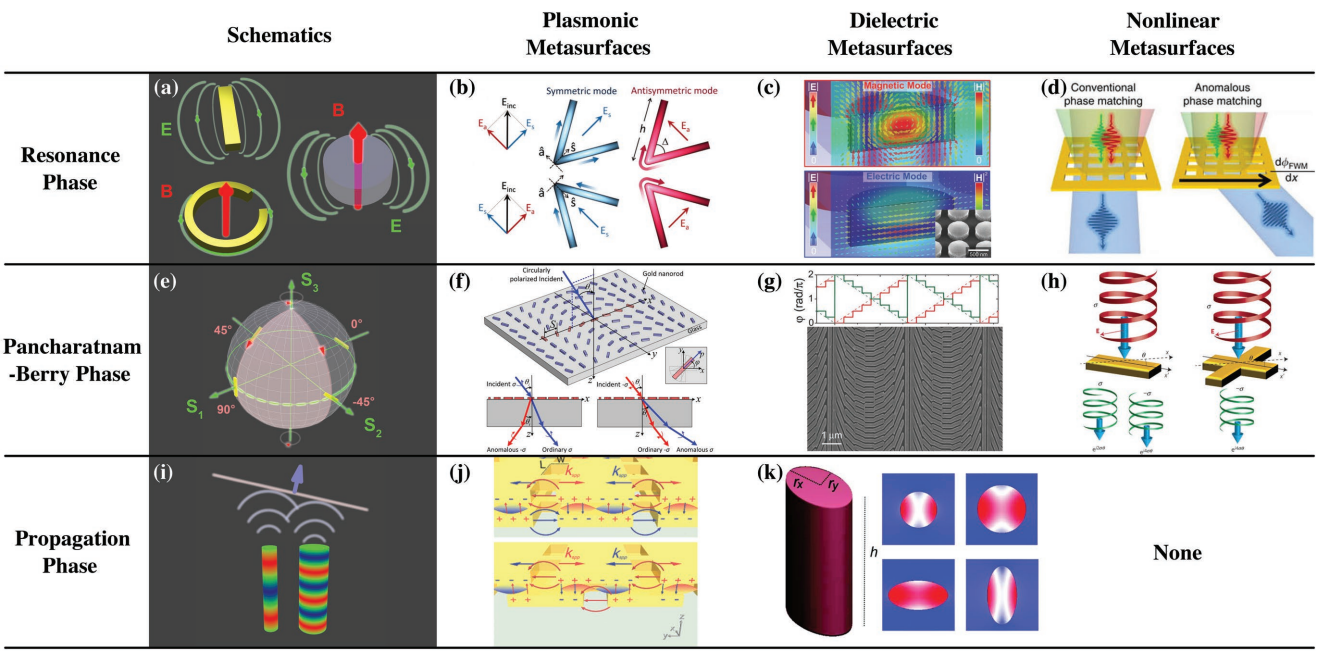

Figure 1. Three basic types of phase discontinuities generated by metasurfaces. a) Schematic representations of the electric fields in plasmonic (left panel) and dielectric (right panel) nanoantennas. Plasmonic rod nanoantennas support only electric resonances while magnetic resonances can be achieved using a split ring resonator (SRR). Dielectric nanoantennas can provide both electric and magnetic resonances. b) V-shaped nanoantennas used to control the propagation direction of linearly polarized light. Reproduced with permission.[4] Copyright 2011, American Association for the Advancement of Science. c) Electric and magnetic field distributions of the magnetic (top) and electric (bottom) dipole mode of a silicon nanodisk metasurface. Inset: scanning electron microscope (SEM) image of a typical nanodisk sample. Reproduced with permission.[30] Copyright 2015, John Wiley and Sons. d) Illustration of the anomalous phase-matching condition for nonlinear phase-gradient metasurfaces containing rectangular nanoapertures. Reproduced with permission.[36] Copyright 2016, Nature Publishing Group. e) Illustration of the geometric phase by parallel transport on a curved surface, which results in a change of phase angle. f) P–B-phase-based metasurface realized by rotated nanorods. Reproduced with permission.[45] Copyright 2012, American Chemical Society. g) Phase profile (top) and SEM image (bottom) of a dielectric gradient metasurface optical element. Reproduced with permission.[52] Copyright 2014, American Association for the Advancement of Science. h) Variety of continuous phase gradients for the third harmonic generation signals generated by unit cells with different rotational symmetries. Reproduced with permission.[56] Copyright 2015, Nature Publishing Group. i) Schematic of the propagation phase. j) Schematic view of the dual-layer metasurface with aligned nanoaperture pairs and with a laterally translated nanoaperture; the surface plasmonic standing wave is shown between the two metallic structures, with the field and charge oscillation indicated. Reproduced with permission.[77] Copyright 2015, John Wiley and Sons. k) Elliptical silicon nanowire scatter used to produce the propagation phase (left) and simulated E_x distributions of four different nanowire geometries (right). Reproduced with permission.[63] Copyright 2011, American Chemical Society.

($\bar{\bar{Z}}_{ms} = j\omega\bar{\bar{\alpha}}_m^{eff}$) can be directly extracted from the complex reflection (R) and transmission (T) coefficients[23]

$$Y_{es} = \frac{2(1-T-R)}{\eta(1+T+R)}, \quad Z_{ms} = \frac{2\eta(1-T+R)}{(1+T-R)} \tag{3}$$

where $\eta = \sqrt{\mu/\varepsilon}$ is the wave impedance of free space. If the normalized electric sheet admittance and magnetic sheet impedance are equal and purely imaginary, then the amplitude of each unit cell's transmission coefficient becomes unity. Additionally, the transmitted phase can be varied anywhere between $-\pi$ to $+\pi$ by adjusting the magnitude of the impedance. The above analysis was implemented in the microwave range with an experimental efficiency of 86%[23] and subsequently extended to the NIR range but with a much lower efficiency due to the weak magnetic response of natural materials and the intrinsic metallic loss of plasmonic elements in this range.[24] A stack of three-layered metasurfaces, which were constructed from a combination of dielectric and plasmonic nanoblocks with various filling ratios and functioned as LC nanocircuit elements, has also been theoretically proposed for light bending in the NIR range with an efficiency of 75%.[25]

Another method to realize Huygens' surfaces is to use all-dielectric nanostructures. Relative to their metallic counterparts, dielectric nanoparticles have two advantages: they exhibit low intrinsic losses, and they can support both electric and magnetic dipolar Mie-type resonances.[26] Figure 1c shows the electric and magnetic field distributions of the magnetic and electric dipole mode of a silicon nanodisk metasurface. For the magnetic dipole mode, we can see a strong magnetic field located in the center of the nanodisk, with a vortex-like electric field distribution around the nanodisk. However, for the electric dipole mode, an electric field maximum can be observed at the center of the nanodisk. Additionally, by tailoring the geometry parameters of the nanostructures, spectrally overlapping electric and magnetic dipole resonances can be achieved with an individual nanostructure to realize zero-backward or zero-forward scattering.[26–31] To understand the physical mechanism of this phenomenon, we can consider an idealized subwavelength array of lossless nanodisk unit cells under plane-wave

illumination. Each individual nanodisk is modeled as electric and magnetic dipoles oriented in orthogonal directions with damping parameters γ_e and γ_m and resonance positions ω_e and ω_m, respectively. The field transmittance and reflection coefficients for this structure can be written as follows[30]

$$t = 1 + \frac{2i\gamma_e\omega}{\omega_e^2 - \omega^2 - 2i\gamma_e\omega} + \frac{2i\gamma_m\omega}{\omega_m^2 - \omega^2 - 2i\gamma_m\omega} \tag{4}$$

$$r = \frac{2i\gamma_e\omega}{\omega_e^2 - \omega^2 - 2i\gamma_e\omega} - \frac{2i\gamma_m\omega}{\omega_m^2 - \omega^2 - 2i\gamma_m\omega} \tag{5}$$

where ω is the frequency of the incident light. Here, the signs of the electric contribution terms in the forward and backward directions are known to be the same, while the signs of the magnetic contribution terms are different in two directions. Therefore, if the electric and magnetic resonances are spectrally overlapped with equal strength and width (i.e., $\omega_e = \omega_m$ and $\gamma_e = \gamma_m$, respectively), then the reflection coefficient is zero, and unit transmission is achieved. Additionally, full 2π phase coverage can be achieved by tailoring the geometry parameters of the nanostructures. Based on this method, multiple types of high-efficiency all-dielectric Huygens' surfaces have been proposed in the NIR region[30,32–34] and the visible region.[35]

The resonance phase has also been extended to the regime of nonlinear metasurfaces. Consider a four-wave mixing (FWM) process in which two transform-limited laser pulses (with ω_j, $\mathbf{k}_j$, and $\mathbf{E}_j(\mathbf{r},t) = \varepsilon_j(\mathbf{r},t)e^{i(\mathbf{k}_j\cdot\mathbf{r}-\omega_j t+\Phi_j)}$, where $j = 1, 2$) interact with a metallic nanoantenna to generate an FWM signal $\mathbf{E}_{FWM}(\mathbf{r},t) = \varepsilon_{FWM}(\mathbf{r},t)e^{i(\mathbf{k}_{FWM}\cdot\mathbf{r}-\omega_{FWM}t+\Phi_{FWM})}$, which travels in the $\mathbf{k}_{FWM}$ direction with frequency $\omega_{FWM} = 2\omega_1 - \omega_2$. A nanoantenna that is much smaller than the wavelength can be approximated by a point dipole (eliminating the position dependence within the antenna). This condition leads to effective fields, $\mathbf{E}_i(\omega_i) = A_i(\omega_i)\varepsilon_i(\omega_i)e^{i\Phi(\omega_i)}$, where $A_i(\omega_i)$ is the field enhancement (a real quantity) and $\Phi(\omega_i)$ is the phase response. Therefore, the third-order polarization is as follows[36]

$$\mathbf{P}^{(3)}(t) \propto \int d\omega_1 \int d\omega_1 \int d\omega_2 \chi_{eff}^{(3)}(\omega_{FWM}, 2\omega_1, -\omega_2) \times |A_1(\omega_1)|^2 A_2(\omega_2)\varepsilon_1(\omega_1)\varepsilon_1(\omega_1)\varepsilon_2^*(\omega_2)e^{i(2\Phi(\omega_1)-\Phi(\omega_2))} \tag{6}$$

where $\chi_{eff}^{(3)}$ is the effective third-order nonlinear susceptibility. The nonlinear FWM signal carries the frequency response at fundamental frequencies through the phase factor $e^{i(2\Phi(\omega_1)-\Phi(\omega_2))}$, which changes sharply for excitations close to the nanoantenna resonance. Based on this theory, the nonlinear phase variation of the FWM signals can cover 2π by finely adjusting the aspect ratio of nanocavity unit cells made of rectangular nanoapertures, as shown in Figure 1d.[36] This strategy can also be applied to the harmonic generation process.[37]

2.2. Pancharatnam–Berry Phase

In addition to introducing variations in the phase based on dispersion of various nanoantennas, a completely different approach is to use the so-called Pancharatnam–Berry phase (P–B phase), which is a geometric phase that arises during adiabatic cycling and can be achieved for scattered light by spatially rotating each unit cell.[38,39] The phase difference between the scattered waves from any two nanoantennas with different rotation angles equals the solid angle enclosed by their corresponding traces in the Poincaré sphere divided by two, as shown in Figure 1e.[40] As an example, two traces start at the north pole of the Poincaré sphere representing right-handed circularly polarized (RCP) incident light, pass different points on the equator that represent two nanoantennas with different rotation angles ($\pi/2$ and $-\pi/4$), and end at the south pole due to the left-handed circularly polarized (LCP) scattered light being monitored. The solid angle enclosed by the two traces is π; thus, the phase difference of the cross-polarized scattered light of the two nanoantennas is $\pi/2$. The main advantage of the P–B phase is that it does not depend on the size of the structures or the inherent material dispersion or structural resonances. The current development of metasurfaces based on the P–B phase has been inspired mainly by the innovative findings that continuous or discrete subwavelength gratings can be used to control the polarization states for the generation of vector beams and the manipulation of wavefronts.[40–42] Consider an anisotropic nanoantenna under normal incidence; as the x- and y-polarizations are decoupled, t_u and t_v characterize the complex coefficient for the incident linearly polarized light along the two principle axes of the nanoantenna. For a nanoantenna with the optical axis rotated by angle θ, the transmission coefficients can be represented using the Jones matrix[43]

$$\hat{t}(\theta) = \hat{R}(-\theta)\begin{pmatrix} t_u & 0 \\ 0 & t_v \end{pmatrix}\hat{R}(\theta) = \begin{bmatrix} t_u\cos^2\theta + t_v\sin^2\theta & (t_u - t_v)\sin\theta\cos\theta \\ (t_u - t_v)\sin\theta\cos\theta & t_u\sin^2\theta + t_v\cos^2\theta \end{bmatrix} \tag{7}$$

where $\hat{R}(\theta)$ is the rotation matrix. Given a circularly polarized (CP) incident wave ($\mathbf{E}_i^{R/L} = (\hat{e}_x \pm i\hat{e}_y)/\sqrt{2}$), the transmitted electric field $\mathbf{E}_t^{R/L}$ can be written as follows[44]

$$\mathbf{E}_t^{R/L} = \hat{t}(\theta)\cdot\mathbf{E}_i^{R/L} = \frac{t_u + t_v}{2}\mathbf{E}_i^{R/L} + \frac{t_u - t_v}{2}e^{\pm i2\theta}\mathbf{E}_i^{L/R} \tag{8}$$

The first term in Equation (8) represents a CP transmitted wave with the same helicity as the incident wave, and the second term represents a CP transmitted wave with the opposite helicity and an additional P–B phase of $\pm i2\theta$, where $\pm$ represents the LCP or RCP light, respectively. Therefore, a phase shift can be tuned from 0 to 2π for the opposite helicity radiation as the anisotropic nanoantenna is rotated from 0 to π. Moreover, the scattering amplitude remains the same due to the unchanged geometry of each unit. Based on this principle, a phase-gradient metasurface that consists of U-shaped nanoapertures was theoretically proposed to steer light into various directions depending on the helicity of the incident light.[44] Gold nanorods were later experimentally used to verify the phenomenon of anomalous refraction, as shown in Figure 1f.[45] Due to the succinct nature of the P–B phase, this concept can be easily extended to other frequencies.[46,47] Several strategies have also

been demonstrated to improve the manipulation efficiency, such as introducing a reflection configuration,[48,49] plasmonic hybridization,[50] and few-layer nanoantennas.[51] A promising way to avoid the Ohmic losses of plasmonic elements is to replace them with dielectric resonators.[52–54] By implementing the P–B phase with silicon nanoantennas (Figure 1g), a high-efficiency anomalous refraction metasurface operating in transmission mode can be achieved in the visible region.[52] By employing graphene-based nanostructures, dynamically tunable anomalous refraction can also be achieved in the infrared regime.[55]

Inspired by the concept of the linear P–B phase, a nonlinear metasurface allowing a continuous control of the phase of the local effective nonlinear polarizability was recently demonstrated, as illustrated in Figure 1h.[56] For a CP fundamental wave propagating along the rotational axis of a unit cell, the local effective nonlinear dipole moment can be expressed as $\mathbf{P}_\theta^{n\omega} = \overleftrightarrow{\alpha}_\theta (\mathbf{E}^\sigma)^n$, where ω denotes the angular frequency of the fundamental beam, $\overleftrightarrow{\alpha}_\theta$ is the nth harmonic nonlinear polarizability tensor of the unit cell with orientation angle θ and $\mathbf{E}^\sigma$ is the electric field of the fundamental wave. As with the linear configuration, $\sigma = \pm 1$ represents the LCP or RCP light, respectively. The nonlinear polarizability of the unit cell can be expressed as $\alpha_{\theta,\sigma,\sigma}^{n\omega} = \mathrm{e}^{(n-1)i\theta\sigma}$ and $\alpha_{\theta,-\sigma,\sigma}^{n\omega} = \mathrm{e}^{(n+1)i\theta\sigma}$ for harmonic generation with the same or opposite helicity, respectively, relative to that of the fundamental wave. The relative phase factors $(n-1)\theta\sigma$ and $(n+1)\theta\sigma$ of the nonlinear waves depend only on the orientation angle of the unit cell. Thus, through the new concept of nonlinear geometric phases, two different continuous phases are imposed on the harmonic generation signals of opposite helicities. Additionally, with the combination of selection rules, only a single or both nonlinear signals can be generated for each harmonic generation process.[57] To increase the nonlinear efficiency of the second harmonic generation (SHG) process, a multi-quantum-well structure can be coupled to each nanoantenna.[58]

2.3. Propagation Phase

In the past few years, a new type of phase shifter, which is characterized by the high aspect ratio of the building block, has been proposed to realize the propagation phase. Distinct from the aforementioned resonance phase, which relies on the abrupt phase change of the resonator, the propagation phase is achieved via the propagation of light in the nanostructure. The phase shifters can be treated as truncated waveguides whose effective refractive indices n_{eff} can be modulated by adjusting the lateral size of structures (Figure 1i). If we neglect the Fabry-Pérot effects, then the accumulated phase shift ϕ_{WG} of a beam passing through a nanostructure with height H can be written as follows[59,60]

$$\phi_{\mathrm{WG}} = \frac{2\pi}{\lambda} n_{\mathrm{eff}} H \tag{9}$$

where λ is the wavelength in free space. If the effective index difference Δn_{eff} between two nanostructures can be modulated to exceed unity, then a phase difference of $\Delta\phi_{\mathrm{WG}} = 2\pi$ is obtained with a subwavelength height. The common phase shifter elements are dielectric ridge waveguides[59,61,62] and high-refractive-index dielectric scatterers.[63–65] The scatterers can be designed to achieve either a polarization-dependent[63,66,67] or a polarization-independent[60,68–70] optical response by changing the cross-section of the structure. The first work on polarization-dependent metalenses based on the propagation phase was reported in ref. [63]. The unit cell is shown in Figure 1k. By changing the geometry parameters of the elliptical silicon nanowire, the mode effective index can be tailored to attain various values. As a result, a variety of propagation phases can be achieved. However, this work realized only two phase levels for each polarization of light, and the efficiencies of these lenses were low. By increasing the phase levels, a polarization-switchable phase hologram with a measured efficiency as high as 91% for a y-polarized beam was realized in the NIR region.[66] A polarization-insensitive metalens using TiO_2 nanopillars with a measured focusing efficiency as high as 90% at a visible wavelength was also demonstrated.[60] Many material systems have been proposed to implement the propagation phase, such as hydrogenated amorphous silicon on a MgF_2 substrate in the MIR,[69] amorphous silicon[61,71] and hydrogenated amorphous silicon on a silica substrate[68] in the NIR, and TiO_2 on a glass substrate or on an aluminum-coated fused silica substrate[70] in the visible region. In the future, we expect additional material platforms to be developed to expand the application areas of the propagation phase.

For metal–insulator–metal (MIM) structures, an accurate propagation constant can be derived by directly solving Maxwell's equations with boundary conditions[72]

$$\tanh\left(\frac{w\sqrt{\beta^2 - \varepsilon_{\mathrm{d}} k_0^2}}{2}\right) = -\frac{\varepsilon_{\mathrm{d}}\sqrt{\beta^2 - \varepsilon_{\mathrm{m}} k_0^2}}{\varepsilon_{\mathrm{m}}\sqrt{\beta^2 - \varepsilon_{\mathrm{d}} k_0^2}} \tag{10}$$

where w is the width of the slit, β is the propagation constant of the surface plasmons, h is the thickness of the metasurface, k_0 is the propagation constant in free space, and ε_{m} and ε_{d} are the permittivities of the metal and dielectric, respectively. Thus, the propagation constant β can be directly modulated using the width of the slit w. The abrupt phase change can be expressed as follows

$$\Phi = \beta d + \alpha = \mathrm{Re}(\beta d) + \arg\left[1 - \left(\frac{1 - \beta/k_0}{1 + \beta/k_0}\right)^2 \exp(i2\beta d)\right] \tag{11}$$

where α is the factor stemming from the multiple reflections of light between the entrance and the interfaces. Clearly, the larger the propagation constant β, the smaller the thickness needed to obtain a local phase shift cover of 0 to 2π, and for a fixed thickness, the phase variation can be achieved by various widths w of each nanoslit. Several nanostructures have been demonstrated to engineer the phase discontinuities based on this concept both in the visible range,[73–75] and the NIR range.[76]

A novel dual-layer metasurface has been proposed recently that can provide simultaneous manipulation of the phase and polarization of the transmitted light, as presented in Figure 1j.[77–79] Surface plasmon polaritons (SPPs) can be excited

at each of the metal–dielectric interfaces by the normally incident light, and a standing wave of SPPs can be formed due to the coupling between the two metal layers resulting in an MIM waveguide. By controlling either the aligned or laterally translated state of the top and bottom nanoapertures, the phase of transmitted light can cover the 0 to 2π range. By exciting the bulk magnetic resonance using antiparallel dipole electric resonances on the sidewalls of thick nanoantennas and the lateral Fabry–Pérot resonance in the cavity containing adjacent thick nanoantennas, high-efficiency phase control in the NIR range has been achieved with plasmonic metasurfaces.[80,81]

3. Basic Applications

3.1. Beam Deflector

The trajectory of a light ray travelling between two points in space can be determined using Fermat's principle. According to this principle, when a plane EM wave impinges on a conventional interface between two homogeneous media, the directions of the reflection and transmission lights are given by Snell's laws. However, if we can create spatial phase variations with a subwavelength resolution along the interface, then we can generalize Snell's laws and control the directions of the reflection and transmission lights at will. The generalized Snell's laws can be written as follows[4,45,82]

$$n_t \sin(\theta_t) - n_i \sin(\theta_i) = \frac{\lambda_0}{2\pi}\frac{d\Phi}{dx} \tag{12}$$

$$n_i \sin(\theta_r) - n_i \sin(\theta_i) = \frac{\lambda_0}{2\pi}\frac{d\Phi}{dx} \tag{13}$$

where n_i and n_t are the refractive indices on the two sides of the interface; λ_0 is the wavelength in a vacuum; θ_i, θ_t, and θ_r are the angles of incidence, refraction, and reflection, respectively (**Figure 2**a); and $d\Phi/dx$ indicates the phase gradient along the interface. One approach to provide the desired phase gradient is to use the resonant phase of metallic antennas. The generalized laws of refraction and reflection were first demonstrated using V-shaped antennas in the MIR region.[4] By changing the geometrical parameters of the V-shaped antennas and using the mirror symmetry counterparts, a 2π phase coverage was achieved for the cross-polarized scattered light. Then, eight antennas with an incremental phase of $\pi/4$ were chosen and equally spaced along the interface at a subwavelength separation. Anomalous reflection and refraction phenomena were then experimentally realized and found to be in excellent agreement with predictions of the generalized Snell's laws. A broadband beam bending was later demonstrated in the NIR region using the same method.[5] When the phase gradient provided by the metasurface is noncoplanar with the plane of incidence, out-of-plane reflection and refraction of light can be achieved.[82] Figure 2b presents the reflection and refraction of light in three dimensions. The phase gradient implemented by the V-shaped antennas forms an angle with respect to the plane of incidence. Therefore, a component of the phase gradient out of the plane of incidence is created, resulting in out-of-plane anomalous reflection and refraction. Anomalous reflection and refraction can also be realized using the P–B phase.[45,46] Zhang et al. proposed a broadband anomalous refraction metasurface based on this method.[45] By arranging the nanorod structures in an array with a constant gradient of the orientation angle along the interface, a broadband anomalous refraction ranging from the visible to the NIR wavelengths was achieved. Additionally, if the rod-to-rod spacing is comparable to the wavelength of light, anomalous diffraction may also occur.[45] The aforementioned methods of using V-shaped antennas and the P–B phase are suitable only for controlling the phase of cross-polarized lights and are challenging to realize high-efficiency beam deflectors. One way around this limitation is to use gap-plasmonic structures.[19,83–85] Figure 2c demonstrates a high-efficiency broadband anomalous reflection metasurface based on gap-plasmonic structures.[19] The unit cell consists of a gold nanorod separated from a back Au film by a MgF_2 spacer. By changing the geometry parameters of the unit cell, this metasurface can realize anomalous reflection with an efficiency up to 80% at ≈850 nm, and the anomalous reflection beam has the same polarization as the incident beam. To realize high efficiency beam deflectors for transmission operations, metasurfaces based on Huygens' surfaces or dielectric structures have been proposed.[23–25,33,35] The first experimental Huygens' surface at optical frequencies was demonstrated in ref. [24]. Using the collocated electric and magnetic polarizabilities, the reflection losses were significantly reduced. However, Ohmic losses remained due to the metallic structures used in the experiment. High-refractive index dielectric structures, due to their low losses and compatibility with existing semiconductor technologies, were later proposed to realize Huygens' surfaces. Figure 2d demonstrates a high-efficiency all-dielectric metasurface in transmission mode.[33] By overlapping the electric and magnetic resonances of the silicon nanoblocks, nearly 100% transmission with a 2π phase control was achieved at telecommunication wavelengths. The measured transmission efficiency of the anomalous refraction was 36%, which is higher than that of most ultrathin plasmonic metasurfaces. Recently, a new metasurface platform based on high-aspect-ratio dielectric structures was proposed.[66,86] In ref. [66], a polarization beam splitter with an experimentally measured efficiency as high as 77% was achieved at an NIR wavelength.

Based on the phase control ability of the metasurfaces, numerous beam deflectors with various functions have been proposed, such as dispersion-free beam deflectors,[62] spectrum splitting surfaces,[85] and linearly polarization beam splitters.[66,87,88] Here, we focus on the discussion of the photonic spin Hall effect (PSHE), which is an important effect realized by metasurfaces. The PSHE is an effect of laterally separating LCP and RCP photons.[86,89–94] Due to the small photon momentum and weak spin–orbit interaction between a photon and its medium, the experimental observation of the PSHE is challenging. However, a metasurface enables the PSHE to be enhanced and directly observed. Figure 2e demonstrates a strong PSHE at a metasurface.[90] A linear phase gradient along the x-direction was produced using V-shaped antennas, which removed the axial symmetry of the system and enhanced the spin-orbit interactions. When linearly polarized light was

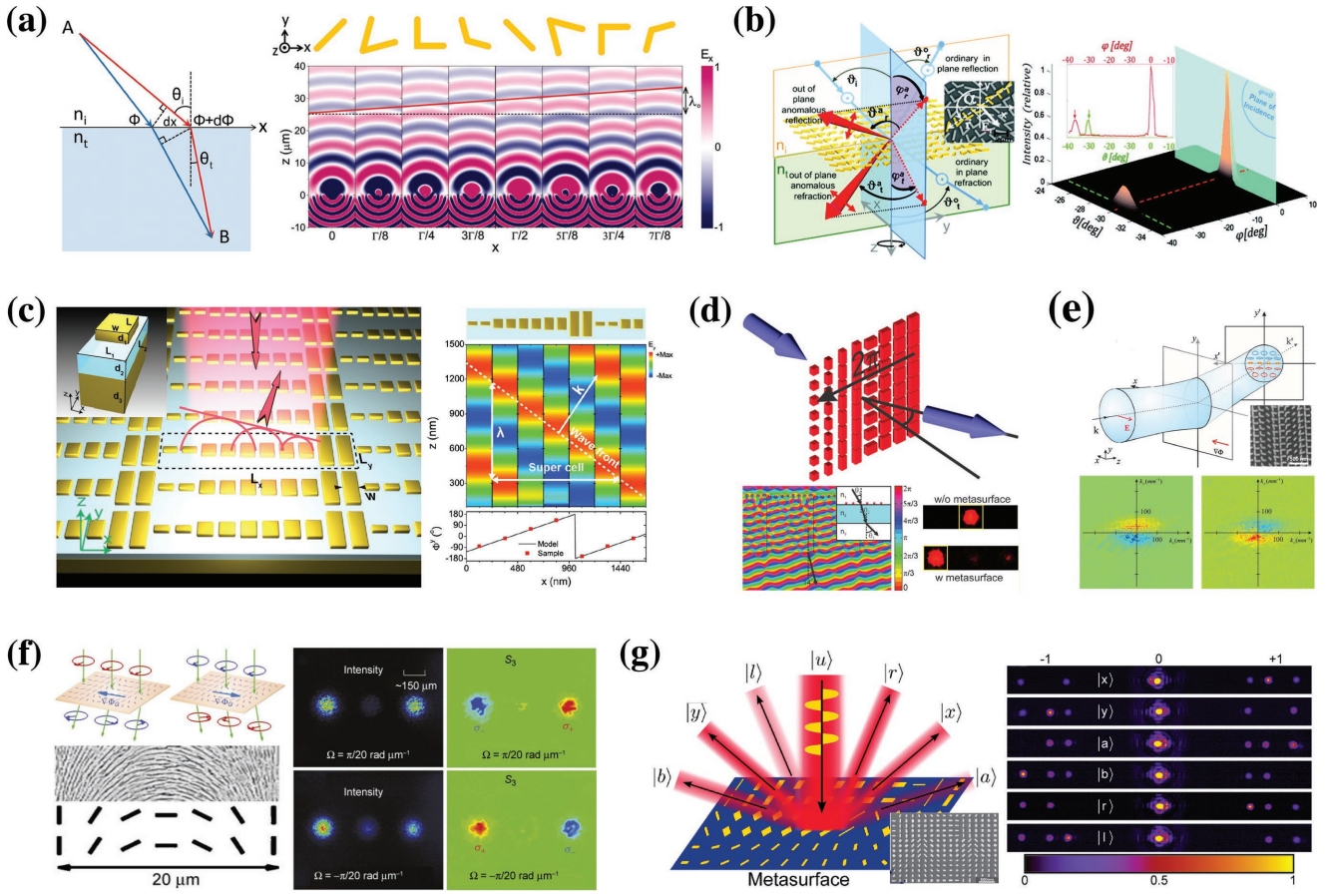

Figure 2. Beam deflectors. a) Schematic of the anomalous refraction (left) and the simulated scattered electric field polarized in the *x* direction for a *y*-polarized plane wave excitation (right). The red straight line in the right panel defines the wavefront, and the plasmonic antennas used in the simulation are shown in the top of the right panel. Reproduced with permission.[4] Copyright 2011, American Association for the Advancement of Science. b) Schematic of the reflection and refraction of light in 3D (left) and the experimental observation of out-of-plane refraction (right). Reproduced with permission.[82] Copyright 2012, American Chemical Society. c) Schematic of a broadband anomalous reflection metasurface (left) and the simulated scattered electric field polarized in the *y*-direction for a *y*-polarized plane wave excitation (right). The antennas used in the simulation and the reflection phase of each unit cell are shown in the top and bottom of the right panel, respectively. Reproduced with permission.[19] Copyright 2012, American Chemical Society. d) Upper panel: schematic of the all-dielectric metasurface for anomalous refraction. Lower panels: simulated phase of the plane wave propagating through the metasurfaces on a SiO_2 substrate (left) and the measured beam positions without and with the metasurface (right). Reproduced with permission.[33] Copyright 2015, American Chemical Society. e) Upper panel: schematic of the PSHE induced by a phase gradient metasurface. Inset: SEM image of the metasurface used in the experiment. Lower panels: measured circular Stokes parameter of the anomalously refracted beam with incidence polarized along the *x*-direction (left) and *y*-direction (right). Reproduced with permission.[90] Copyright 2013, American Association for the Advancement of Science. f) Left panels: schematic of the PSHE induced by a metasurface with a spin-dependent P–B phase gradient (top) and the detailed geometry of the metasurface (bottom). Measured intensities (middle panels) and S_3 parameters (right panels) after a linearly polarized beam passes through two metasurfaces with opposite rotational rates. Reproduced with permission.[92] Copyright 2015, Nature Publishing Group. g) Left panel: schematic of the working principle of a metagrating. Inset: SEM image of the metagrating used in the experiment. Right panels: normalized optical images of the diffraction spots. The incident polarization state is denoted by $|u\rangle$ in each panel. Reproduced with permission.[96] Copyright 2015, Optical Society of America.

incident on the metasurface, the light of the opposite CP state accumulates at the opposite edges of an anomalously refracted beam in the transverse direction. This strong PSHE occurred in real space and was observable by directly measuring the transverse motion. The PSHE can also be realized in momentum space. Figure 2f demonstrates a giant PSHE using the P–B phase at a visible wavelength.[92] By locally varying the optical axis direction of the dielectric metasurface, a spin-dependent separation in momentum space is observed. According to the mapping relationship between real space and momentum space, the induced real-space shift increases linearly during beam propagation. Therefore, this method offers a convenient way to magnify the PSHE and facilitate the direct measurement. In principle, the PSHE can be realized with ≈100% efficiency by using the metasurfaces.[91] Two reflective metasurfaces showing ≈90% efficiencies for the PSHE in the microwave region were also experimentally demonstrated.[91] Recently, Chen et al. achieved a relatively large PSHE in refraction with an efficiency exceeding 70% at an NIR wavelength using a gold-nanorod-based metasurface.[80] In view of the metasurfaces' capability to split different polarized light into different directions, one important application for beam deflection is polarization state

measurements.[95–97] Figure 2g demonstrates a plasmonic metasurface for the simultaneous determination of the Stokes parameters.[96] By interweaving three types of phase gradient metasurfaces into a metagrating, the state of polarization of the incident light can be determined through simultaneously measuring the six correspondent diffraction intensities that reveal the Stokes parameters of the light. An in-line polarimeter that can perform nondestructive polarization measurements of optical signals at telecommunication wavelengths was designed.[97] It was realized by detecting the highly polarization-dependent scattered field of a metasurface in four directions. More complex functions, such as spectropolarimeters,[98,99] can also be realized based on metasurface beam deflectors.

3.2. Metalenses

Conventional lenses based on the phase accumulation along the optical path are often bulky and heavy, imposing a significant challenge on their integration with other optical devices. Metasurfaces offer an opportunity to overcome these limitations. We can realize a metalens by imposing the following parabolic transmission/reflection phase profile on the metasurfaces

$$\varphi(x,y) = -\frac{2\pi}{\lambda}\left(\sqrt{x^2+y^2+f^2} - f\right) \tag{14}$$

where x and y are the coordinates of the phase-shifting elements of the metasurface, λ is the wavelength in free space, and f is the focal distance of the lens. **Figure 3** shows selected examples of planar metalenses. The early works on metalenses consisted predominantly of plasmonic structures.[44,100–104] Figure 3a presents a metalens that is free of spherical aberration at telecom wavelengths.[100] The desired phase profile was implemented using carefully designed V-shaped plasmonic antennas. An alternative method to realize metalenses is to use the P–B phase.[44,46,101,103] Figure 3b presents a dual-polarity plasmonic metalens operating at visible wavelengths. Due to the nature of the P–B phase, by controlling the helicity of the input light, the positive and negative polarities are interchangeable in a single metalens.[101] Apart from the plasmonic antennas, the aperture configurations can also be used to create metalenses.[44,104] However, the focusing efficiency of these plasmonic metalenses is relatively low at visible and NIR wavelengths for transmission operation as a result of Ohmic losses and a small scattering efficiency. Additionally, achieving 2π phase delays in co-polarization is challenging when using ultrathin transmit arrays.[105] To address these problems, researchers have begun to use dielectric structures to create metalenses.[52,54,60–62,66,68,69,106–111] Figure 3c presents a sub-wavelength-thick lens with high numerical apertures (NAs) and a large efficiency based on high-contrast transmission arrays at NIR wavelengths.[68] The metalenses are polarization-insensitive due to the circular amorphous silicon post configurations. The measured focusing efficiency is as high as 82%. A similar metalens was later designed for visible wavelengths using TiO_2 nanopillars.[60] The focusing efficiency was measured to be as high as 90% with an NA of 0.6 at the designed wavelength of 660 nm. Figure 3d presents metalenses with an NA of 0.8 and efficiencies as high as 86% at visible wavelengths.[53] The desired phase profile is implemented by rotating high-aspect-ratio TiO_2 nanofins. Diffraction-limited focusing and subwavelength resolution imaging are achieved with image qualities comparable to that of a state-of-the-art commercial objective lens. Based on the P–B phase, these high-aspect-ratio nanostructures can enable many high-efficiency chirality dependent metalenses with novel functions, such as multispectral chiral imaging,[54] chiral spectrometer,[106,108] and immersion metalenses.[112]

Stimulated by multiple applications, various metalenses have been proposed in recent years, such as multifocal metalenses,[113,114] 3D metalenses,[115] metalens doublets,[116,117] and Fourier metalenses.[118] Chen et al. proposed a Fourier metalens that can perform a Fourier transform for a large incident angle range and a broad operating bandwidth.[118] Multiple efforts are underway to develop tunable and reconfigurable metalenses using mechanical[119,120] or optical control.[121] Figure 3e presents an optically reconfigurable metasurface based on phase-change materials.[121] With tailored trains of femtosecond pulses, the complex refractive index profiles of $Ge_2Sb_2Te_5$ (GST) films can be written, erased and rewritten. Various optical components, such as chromatically corrected focusing zone plates and super-oscillatory lenses, can be written with a high accuracy based on this method. In particular, a dynamically optically reconfigurable zone-plate device was achieved by reamorphization and re-crystallization of Fresnel zone patterns. Controlling the chromatic dispersion of lenses is of great significance in multiple applications, including imaging and microscopy. Recently, many efforts have been made to realize achromatic metalenses.[61,62,70,71,122–126] In general, to realize equal focal lengths at various wavelengths, a wavelength-dependent phase profile should be imposed on the metasurface to compensate for the phase differences accumulated during propagation through free space. Figure 3f presents an achromatic lens operating at three wavelengths in the NIR region.[61] The required dispersive phase compensation was achieved using an aperiodic array of coupled dielectric nanoresonators. A polarization-insensitive metalens with the same focal distance at 1550 and 915 nm was subsequently demonstrated in ref. [71]. The desired phase profiles at various wavelengths were implemented using unit cells with multiple dielectric structures. More recently, Capasso et al. demonstrated a reflective achromatic metalens with >60 nm bandwidth in the visible region,[70] which was accomplished by dispersion engineering of dielectric phase shifters that provided both multiple 2π phase coverage and anomalous dispersion. Tsai et al. demonstrated broadband achromatic metalenses in the NIR region for CP incidences in a reflection scheme (see Figure 3g).[123] The basic phase profile for a metalens was implemented using the P–B phase. The phase compensations for various wavelengths were acquired by suitably designing the resonance phase of each unit element. Except for the phase compensation method, which typically requires that each unit cell compensates the phase for all desired wavelengths, we can also realize achromatic metalenses by designing a variety of structures for various wavelengths and combining them. Figure 3h presents a stacked multilayered achromatic lens for red, green and blue light in the visible region.[126] The metalens is composed of three dense vertical stacked metasurfaces, where each layer is fabricated from various materials and with various design parameters for a specific spectral band. The

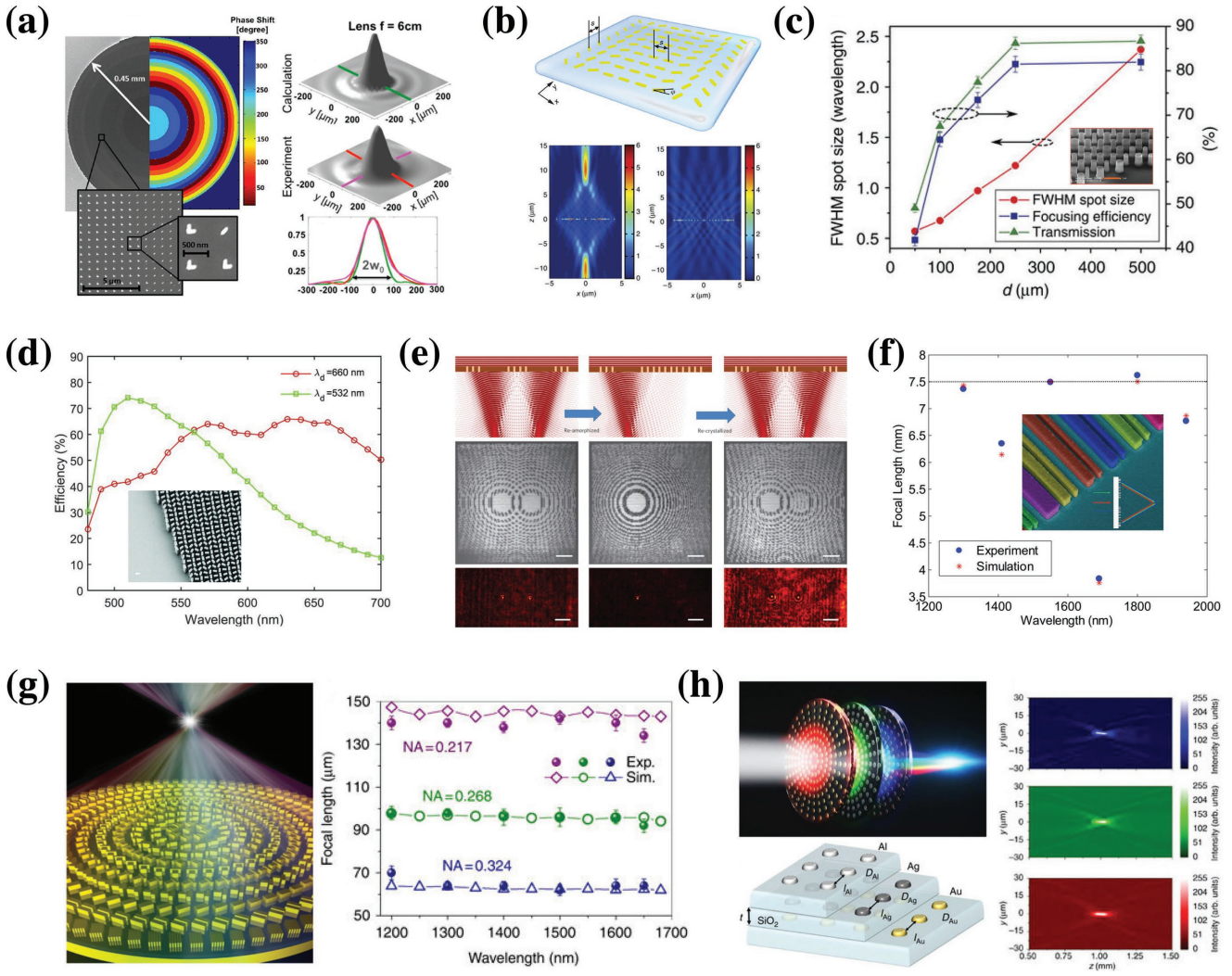

Figure 3. Metalenses. a) Left panel: SEM image of a plasmonic metalens consisting of V-shaped nanoantennas. The corresponding phase shift profile is shown on the right. Right panels: simulated (top) and measured (middle) transverse cross-sections of the intensity profile. The line scans of these two transverse cross-sections are shown in the bottom of the right panels. Reproduced with permission.[100] Copyright 2012, American Chemical Society. b) Upper panel: schematic of a bipolar plasmonic metalens. Lower panels: simulated intensity distributions of the metalens with RCP (left) and LCP (right) incident light. Reproduced with permission.[101] Copyright 2012, Nature Publishing Group. c) Measured plane of focus full width at half maximum (FWHM) spot size, transmission and focusing efficiency of high-contrast transmission array metalenses as a function of their focusing distance. Inset: SEM image of the silicon posts forming the metalenses. Reproduced with permission.[68] Copyright 2015, Nature Publishing Group. d) Measured focusing efficiency of metalenses. Inset: SEM image of the TiO_2 nanofins forming the metalens. Reproduced with permission.[53] Copyright 2016, American Association for the Advancement of Science. e) Dynamically optically reconfigurable zone-plate device that can form two different foci (left) and then erase one focus (middle) and subsequently restore it (right). Reproduced with permission.[121] Copyright 2016, Nature Publishing Group. f) Measured and simulated focal lengths of a multiwavelength achromatic lens for several wavelengths. Inset shows a false-colored SEM image of the metalens. Reproduced with permission.[61] Copyright 2015, American Chemical Society. g) Schematic of a broadband achromatic metalens (left) and the measured and simulated focal lengths with various NA values (right). Reproduced with permission.[123] Copyright 2017, Nature Publishing Group. h) Left panels: schematic of a three-layer multispectral achromatic lens (top) and schematic of the detailed geometry of the layered structure (bottom). Right panel: measured intensity distributions of the focal region for the achromatic lens. Reproduced with permission.[126] Copyright 2017, Nature Publishing Group.

focal length of each layer can be designed independently; thus, both achromatic lenses and anomalous dispersive lenses can be achieved based on this spatial multiplexing method. Achromatic metalenses can also be achieved by overlapping two or more long-depth-of-focus foci or by overlapping the discrete foci of different wavelengths.[124] Using the principle of superoscillations, achromatic subdiffraction photonic focusing metalenses were realized in both the NIR and the visible region.[124] In particular, this method can create foci with sizes smaller than the Abbe-Rayleigh diffraction limit. Even though multiple studies have addressed the chromatic aberration problem under the framework of metalens, much work remains before high-efficiency broadband achromatic metalenses that can be used in practice are ultimately achieved, particularly in the visible region. In view of the potential abilities of metasurfaces to control the phase and dispersion of unit cells independently,[122] numerous high-efficiency metalenses with novel functions are foreseeable in the future.

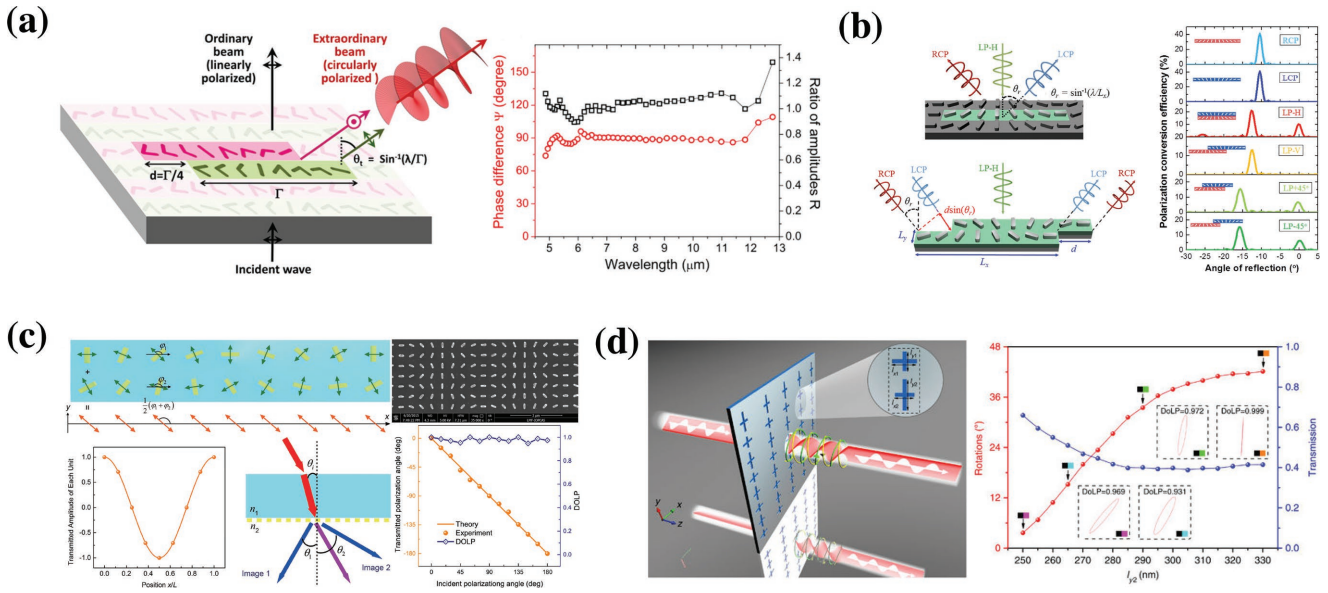

Figure 4. Polarization manipulators based on gradient metasurfaces. a) Left panel: schematic of a background-free quarter-wave plate consisting of two V-shaped antenna subunits. Right panel: simulated phase difference and ratio of amplitudes between the two orthogonal, linearly polarized waves as a function of wavelength. Reproduced with permission.[127] Copyright 2012, American Chemical Society. b) Schematic of polarization generators (left) and the simulated conversion efficiency for each polarization (right). Reproduced with permission.[128] Copyright 2017, American Chemical Society. c) Left panels: schematic of a metasurface half-wave plate with a constant optical axis (top), transmission amplitude of each unit-cell as a function of position (left bottom) and schematic of the different propagation directions of the object and the image light (right bottom). Right panels: SEM image of a half-wave plate with the optical axis along the *x*-axis (top) and the transmitted polarization angle of the image light as a function of the incident polarization angle (bottom). Reproduced with permission.[130] Copyright 2017, American Chemical Society. d) Schematic of the optical activity process with a nonchiral metasurface (left) and the calculated optical rotations and amplitude transmissions as a function of a geometrical parameter (right). Reproduced with permission.[132] Copyright 2016, Nature Publishing Group.

3.3. Polarization Manipulator Based on Phase Modulation

The arbitrary polarization manipulation of EM waves based on metasurfaces has attracted much attention in the scientific community because of the wide range of modern optical applications that such control can afford. One way to realize polarization manipulators, such as quarter-wave plates, half-wave plates, and optically active devices, is to use metasurfaces comprising periodic strongly scattering anisotropic nanostructures that can abruptly change the polarization of light. However, these devices are based on the relatively narrow resonance of the unit cell structures, which limits their working bandwidth. Moreover, the performance of these devices is typically degraded by the optical background that cannot be converted to the desired polarized light. One method to solve these problems is to use spatially inhomogeneous arrays of anisotropic optical antennas. **Figure 4**a presents a broadband, background-free quarter-wave plate in the MIR wavelength range.[127] Two subunits (pink and green), each of which contains eight gold V-shaped antennas, make up a unit cell. The offset between the subunits introduces a $\pi/2$ phase difference between two copropagating waves (co-PWs) with equal amplitudes and orthogonal linear polarization. As a result, a CP extraordinary beam can bend away from the surface normal in the far field, leading to background-free polarization conversion. This method can realize a broadband wave plate because the method is less sensitive to wavelength variation. Additionally, this method can independently modulate the phase difference between two orthogonal polarizations and can thus generate scattered light waves with arbitrary polarization states. This capability was later demonstrated using a reflective aluminum plasmonic metasurface in the visible region.[128] Figure 4b presents the reflective polarization generator that can produce any polarized beam with linearly polarized incident light. Using the P–B phase, linearly polarized incident light can be decomposed into two orthogonal CP light beams that are bent in two different directions. The offset between the nearby subunits introduce the desired phase difference between the LCP and RCP light that is reflected to the same anomalous angle. The superposition of the two CP light beams in the far field can produce light of any desired polarization. By integrating six different areas into one metasurface, each with a specific polarization conversion function, the polarization generator can simultaneously produce four different linearly polarized beams and two orthogonal CP beams. A similar metasurface using the resonant phase was demonstrated in ref. [129] for the Ku-band. By designing the anisotropic reflection-phase distributions along the x and y directions, the x- and y-polarized components of a linearly polarized point source can be independently manipulated to realize multibeam reflections. When the x- and y-polarized reflected beams are designed to deflect to the same direction with equal amplitudes, the polarization state of the reflected wave is controlled solely by the phase difference between the beams. However, this structure is limited to producing a fixed polarization state for a specific arrangement. Recently, Chen et al. proposed a method to design broadband half-wave plates that can change the polarization angle from θ to $-\theta$ with respect to the optical axis for any

polarization.[130] Figure 4c presents the unit cell of the half-wave plates. By properly arranging the two subunits that are rotating in different directions, the metasurfaces can separate the transmitted object (purple) and the image (blue) light using the amplitude modulation. The two nanoantennas in the same column form a nanoantenna pair. The angular bisector of the nanoantenna pairs (the optical axis of the half-wave plate) remains constant during the rotation. The polarization conversion angle is wavelength-independent and can be exactly predicted using a classical half-wave plate. By modulating the phase differences between two or more subunits, an optical activity can also be realized using nonchiral metasurfaces.[131–133] Kildishev et al. demonstrated a broadband optically active metasurface that can rotate linearly polarized light by 45° in the NIR region.[131] The fundamental mechanisms of the optical activity is the same as in ref. [128]. Figure 4d presents a controllable optical active metasurface with nonchiral plasmonic structures.[132] The unit cell contains two different cross-shaped nanoaperture subunits that can convert the linearly polarized light into RCP or LCP light at a subwavelength scale. Simultaneously, by adjusting the geometric parameters of the nanostructures, the phase difference between the RCP and LCP lights can be modulated from $\approx\pi/2$ to π, leading to a continuously controllable optical activity from 3° to 42°. The method of using spatially inhomogeneous arrays of anisotropic optical antennas provides a flexible tool to modulate the phases of different polarized lights. In particular, this method facilitates the realization of dynamical control of polarization states by hybridizing metasurfaces with phase-change materials.[134] However, the efficiency of the polarization manipulation requires further improvement. Such improvements might be enabled by using dielectric structures or hybrid dielectric-metal structures. Based on the phase modulation of metasurfaces, we expect more polarization manipulators with various functions to be developed.

3.4. Optical Vortex

An optical vortex beam is a type of beam with a doughnut-shaped intensity profile and a helical phase front carrying orbital angular momentum (OAM).[135,136] The phase profile can be written as follows: $\varphi = l\theta$, where l is the topological charge and θ is the azimuthal angle in the plane perpendicular to the propagation direction; l can be viewed as the number of twists within one wavelength and is related to the orbital angular momentum L by the equation $L = l\hbar$, where $\hbar$ is the reduced Planck constant. An optical vortex can be produced by imposing an azimuthally varying phase profile on the metasurfaces using either the resonant phase[4,137,138] or the P–B phase.[45,139–142] **Figure 5**a presents a vortex beam generator based on V-shaped

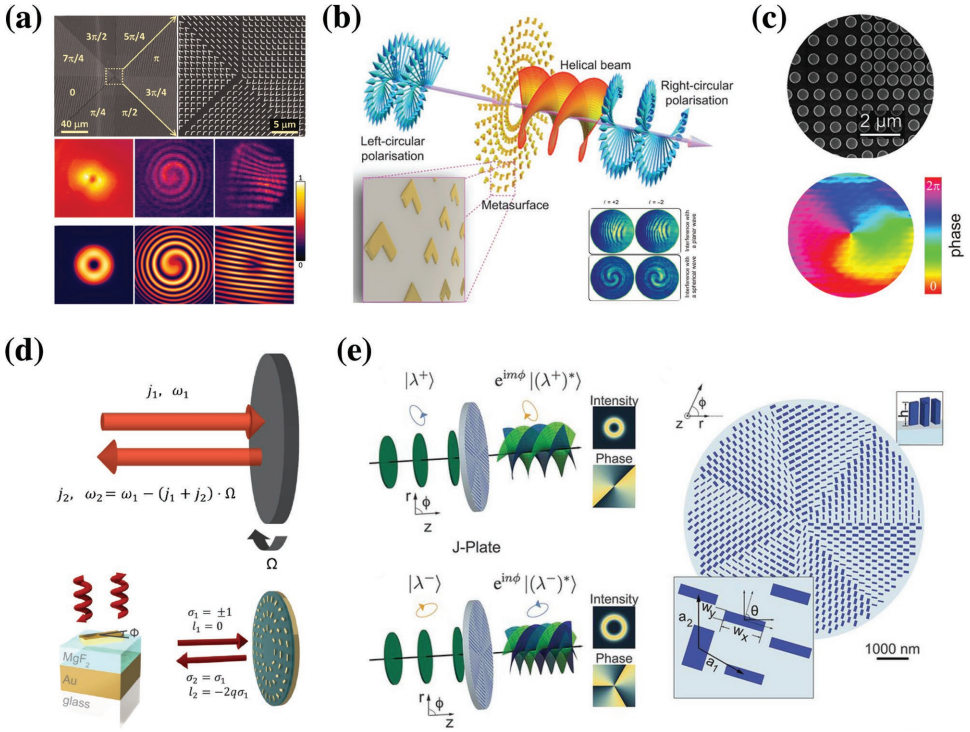

Figure 5. Optical vortices. a) Upper panel: SEM image of the plasmonic vortex beam generator. Lower panels: measured and calculated far-field intensity distributions of the vortex beam (left) and measured and calculated interference patterns created by the interference of an optical vortex and a copropagating Gaussian beam (middle) or a tilted Gaussian beam (right). Reproduced with permission.[4] Copyright 2011, American Association for the Advancement of Science. b) Schematic of the spin–orbit coupling through a plasmonic metasurface. Inset: interference pattern of the generated vortex beams with planar and spherical waves. Reproduced with permission.[139] Copyright 2014, Nature Publishing Group. c) SEM image of the silicon metasurface and reconstructed phase of the object beam. Reproduced with permission.[34] Copyright 2015, American Chemical Society. d) Schematic of the rotational Doppler shift induced by the spinning metasurfaces. Reproduced with permission.[147] Copyright 2017, Optical Society of America. e) Schematic of the arbitrary spin-to-orbital angular momentum conversion (left) and the typical J-plate design (right). Reproduced with permission.[148] Copyright 2017, American Association for the Advancement of Science.

plasmonic antennas.[4] The plasmonic pattern consists of eight regions, each designed to impart a constant phase to the incident planar light, providing an azimuthally varying phase from 0 to 2π. As a result, an optical vortex with $l = 1$ is generated, which can be identified by the interference with a Gaussian beam. When a copropagating Gaussian beam interferes with the vortex beam, a spiral interference pattern is produced. When a Gaussian beam and the vortex interfere at a small angle, a dislocated interference fringe is produced. Figure 5b presents a vortex beam generator based on the P–B phase at visible wavelengths.[139] By arranging the orientation angles of the plasmonic gold nanoantennas in a way that rotates 2π along a path surrounding the plate origin, an azimuthally varying phase from 0 to 4π is imparted to the converted CP light. Due to the nature of the P–B phase, the topological charges of the generated optical vortices are spin-dependent. That is, for LCP and RCP input beams, the topological charges of the generated optical vortices are $l = +2$ and $l = -2$, respectively. This finding can be verified by examining the interference pattern of the generated optical vortices with planar waves and spherical waves. An optical vortex can also be produced using fork gratings.[143,144] A vortex beam generator based on fork gratings was demonstrated in ref. [144]. The fork-type phase distribution can be viewed as the superposition of a linear-gradient phase and an azimuthally varying phase. Therefore, the device can not only produce the optical vortices but can also simultaneously control their directions. The phase profile is encoded into the metasurface using aluminum nanoslits with various orientation angles. When the metasurface is illuminated with a linearly polarized Gaussian beam, different CP vortex beams with different topological charges are deflected to different directions. However, the efficiency of these plasmonic metasurfaces is relatively low. One way to improve the efficiency is to use the dielectric structures to generate optical vortices.[33,34,145,146] Figure 5c presents a polarization-independent silicon metasurface for high-efficiency optical vortex generation at telecom wavelengths.[34] By overlapping the electric and magnetic dipolar resonances of the silicon nanodisks, a high-efficiency Huygens' metasurface is achieved. The required spatial distribution phase is achieved by changing the lattice spacing of the nanodisk arrays. A transmission efficiency exceeding 70% can be achieved in this experiment. The phase gradient metasurfaces can easily transfer different OAM to a beam, which facilitates the study of the influence of complex momentum coupling. Recently, Zentgraf et al. demonstrated the rotational Doppler shift induced by spin-orbit coupling of light at spinning metasurfaces.[147] As shown in Figure 5d, a q-plate is constructed using the P–B phase encoded by gap-plasmonic structures. A CP light is reflected into the cross-polarization, and its OAM is changed by the metasurface. When a metasurface rotates at a constant angular frequency, the frequency of the reflected CP light is changed due to the rotational Doppler effect. The frequency shift can be measured by measuring the time-dependent interference signal. The experiments demonstrate that the Doppler shift is proportional to the rotational angular frequency of the metasurface and the total amount of transferred angular momentum. This effect may find uses in the remote detection of spinning objects. More recently, Capasso et al. proposed a method to realize the arbitrary spin-to-orbital angular momentum conversion of light. To realize this function, the metasurface should be able to simultaneously control the orientation angle of the fast axis and phase shifts. The structures of the metasurface are shown in Figure 5e. The phase shifts of the light that is linearly polarized along the symmetry axes of the elements are controlled by varying the length and width of the TiO_2 nanofins, and the orientation angles of the nanofins are simultaneously varied azimuthally. As an example, a metasurface that can convert LCP and RCP light into optical vortices with various values of the OAM was designed and experimentally verified. An optical vortex can also be manipulated by nonlinear metasurfaces. A spin-controlled OAM of light in SHG using ultrathin photonic metasurfaces has been proposed; the spin manipulation of the OAM mode of the harmonic waves was directly verified using the SHG from a gold unit cell with threefold rotational symmetry.[149] By creating metasurface-based nonlinear computer-generated holograms (CGHs), vortex beams at SHG were also demonstrated, and the diffraction angle of the beam was scanned by changing the pump wavelength.[150] Additionally, optical vortex generation combined with other functions is discussed in Section 4.3.

3.5. Other Applications in Beam Manipulation or Control

With the development of metasurfaces and other technologies in the fields of photonics and nanoscience, numerous applications based on phase gradient metasurfaces have been proposed. In addition to the basic applications mentioned above, we review selected additional important applications in this section.

In the past few years, we have witnessed the expansion of metasurfaces from plane geometry to nonplanar geometry, which has developed into a new research direction named metasurface cloaks.[151–155] **Figure 6**a shows an ultrathin, invisibility skin cloak for a visible wavelength.[151] Using a method of phase compensation that uses the gap-plasmonic structures, the skin cloak can completely reshape the phase of the reflected light, as if the light were reflected from a flat mirror. This type of skin cloak can hide an arbitrarily shaped 3D object but works at a specific wavelength only and produces a specific wavefront. Subsequently, Genevet et al. proposed a design theory for metasurfaces with arbitrary geometries.[152] The theory, called conformal boundary optics, allows one to design the transmission and reflection at will for any arbitrary interface. Faraon et al. demonstrated a conformal flexible dielectric metasurface that can decouple the optical properties of objects from their physical shape.[156] For example, cylindrical lenses covered with this metasurface can be transformed to function as aspherical lenses that focus light to a point. Recently, Luo et al. proposed a method to realize a reconfigurable metasurface cloak for dynamical illusions at a microwave frequency.[153] By reconfiguring the phase distribution of the reflection beam using the varactor configurations, the cloak can not only generate a mirror-reflection wavefront but can also dynamically generate other illusions.

A nondiffracting Bessel beam, as one of the exact solutions of the free-space Helmholtz equation, was first demonstrated in 1987 with a transverse intensity profile that can be described by the Bessel functions of the first kind. Many notable properties have been revealed since its discovery, such as nondiffraction

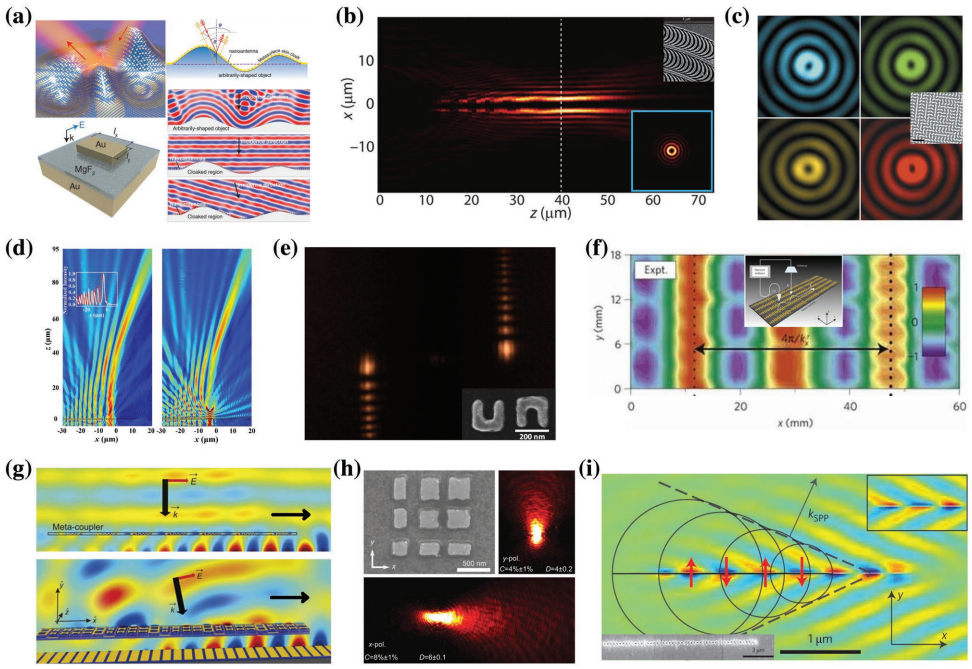

Figure 6. Selected additional applications realized with metasurfaces. a) Left panels: 3D schematic of a metasurface skin cloak (top) and the unit cell used to build the metasurface (bottom). Right panels: schematic of a cross-section of the metasurface (top) and the simulated electrical field distributions based on an actual design (other panels). Reproduced with permission.[151] Copyright 2015, American Association for the Advancement of Science. b) Measured cross-polarized intensity distribution of a higher-ordered Bessel beam generated by metasurfaces similar to the natural catenaries. Inset: SEM image of the fabricated metasurface. Reproduced with permission.[158] Copyright 2015, American Association for the Advancement of Science. c) Measured intensity profiles of wavelength-independent Bessel beams with a high NA generated by a dielectric metasurface. Inset: SEM image of the fabricated metasurface. Reproduced with permission.[159] Copyright 2017, Nature Publishing Group. d) Simulated electric field distribution of the generated Airy beam (left panel) and its self-healing property (right panel) with both its phase and simplified amplitude modulation. Reproduced with permission.[164] Copyright 2016, John Wiley and Sons. e) Far-field second-harmonic Airy beams at first-order diffraction generated by SRRs. Inset: SEM image of part of the fabricated metasurface. Reproduced with permission.[150] Copyright 2016, American Chemical Society. f) E_z distribution on part of the metasurface that can convert PWs to surface waves (SWs). Inset: schematic of the sample and the near-field scanning technique. Reproduced with permission.[169] Copyright 2012, Nature Publishing Group. g) Simulated H_y distributions in the case of SPP excitation by the metacoupler under a normally incident beam (top) and an obliquely incident beam (bottom). Reproduced with permission.[171] Copyright 2016, Nature Publishing Group. h) SEM image of a plasmonic coupler (left top) and the leakage radiation microscopy images showing SPP excitation along the *y*-direction for *y*-polarized light (right top) and the *x*-direction for *x*-polarized light (bottom). Reproduced with permission.[175] Copyright 2014, Nature Publishing Group. i) Simulated Cherenkov surface plasmon wakes generated by a 1D array of aperture antennas under an obliquely incident beam. Inset: SEM image of the nanostructures used in the experiment. Reproduced with permission.[176] Copyright 2015, Nature Publishing Group.

and self-healing.[157] Conventional methods to generate zeroth-order Bessel beams use a conical prism or an objective paired with an annular aperture. By substituting metaaxicons for the conventional axicons, both zeroth-ordered and higher-ordered Bessel beams can be generated by integrated metadevices with a high NA. Using V-shaped nanoantennas, a zeroth-ordered Bessel beam was achieved at telecom wavelengths but with a low efficiency.[100] High-efficiency zeroth-ordered and higher-ordered Bessel beams were subsequently generated in the visible spectrum with a dielectric metasurface[52] and metallic structures similar to the natural catenaries (Figure 6b).[158] Metaaxicons with a high NA of up to 0.9 were demonstrated recently that can generate both zeroth- and higher-ordered Bessel beams, as shown in Figure 6c.[159] Additionally, the FWHM of the generated Bessel beams was experimentally provided that was independent of the wavelength by tailoring the phase profile of the metaaxicons. In addition to conventional Bessel beams, vector Bessel beams were also exploited by superimposing the Bessel profiles with cylindrical vector beams.[160] Gaussian beams with linear or circular polarization can both be converted into vector Bessel beams, and the reciprocal process was also demonstrated, that is, that vector Bessel beams can be transformed into collimated, scalar beams with linear and circular polarizations.

The discovery of Bessel beams aroused an enthusiasm for exploring additional nondiffracting wave profiles conforming to the Helmholtz equation. The nondispersion Airy wave packet was first predicted in 1978 by demonstrating that the Schrödinger equation can possess an Airy function form solution.[161] Inspired by the mathematical similarity between the Schrödinger equation and the paraxial Helmholtz equation, the Airy beam was first demonstrated in the optical domain in 2007.[162,163] In addition to the nondiffracting and self-healing features, an Airy beam has the remarkable feature, unlike the Bessel beam, of freely accelerating even in the absence of any external potential. However, conventional methods to generate an Airy beam typically involve the Fourier transform of a lens, which necessitates at least one focal length, thus affecting the compactness of the optical system. By employing orthogonal nanorods, a simplified metasurface was theoretically proposed to

generate 1D plasmonic Airy beams using both phase and amplitude modulation, as illustrated in Figure 6d.[164] The bending degree of the generated Airy beam can also be easily controlled by changing the number of nanorods. Experiments of transmission-type Airy beams were subsequently demonstrated by simultaneously tailoring the amplitude and phase of a metallic C-aperture array.[165] The nondiffracting Airy beams can also be generated in the terahertz (THz) range and even to be dual-wavelength.[114,166] By manipulating both the phase and amplitude of the quadratic nonlinear coefficient locally at the single inclusion level, emitted second harmonic Airy beams from nonlinear binary phase CGHs were also demonstrated, as presented in Figure 6e.[150] In addition to launching Airy beams in free space, Airy plasmons have also been excited by an engineered nanoscale phase grating and a graded nanocave array.[167,168]

Phase gradient metasurfaces can also act as bridges linking PWs and SWs.[169] As shown in Figure 6f, the reflection phase gradient provides a transverse wave vector that can compensate the momentum mismatch between a PW and an SW, resulting in a nearly perfect PW-to-SW conversion for any incidence angle larger than a critical value. Broadband and high-efficiency conversion from guided waves to spoof SPPs in the microwave frequency has also been realized.[170] This conversion was implemented using gradient grooves and a flaring ground to simultaneously match the momentum and impedance of a conventional coplanar waveguide and a plasmonic waveguide. Recently, Zhou et al. demonstrated a high-efficiency surface plasmon metacoupler in the microwave regime.[171] By placing a transparent gradient metasurface above the target plasmonic metal at a certain distance, an experimental efficiency of ≈73% was achieved for the PW-to-SPP conversion due to the suppression of both decoupling and surface reflections (Figure 6g). The phase gradient metasurface not only can act as a coupler to connect a PW and an SW, but also can control the propagation of SWs.[172,173] By patterning an interference pattern of the incident vortex beam and focused SPP on a plasmonic interface, an incident vortex beam that carries OAM can be transferred into focused SPP waves, which can be used to detect the OAM of light.[172] By applying the P–B phase on a metal film, we can realize a helicity-dependent directional SPP excitation[173] or a helicity-dependent near-field intensity distribution.[174] Figure 6h shows a plasmonic coupler that can realize a unidirectional polarization-controlled SPP excitation at telecom wavelengths.[175] By independently manipulating the orthogonal polarizations of reflected light with gap-plasmonic structures, various types of linearly polarized incident light can be converted into SPPs propagating in orthogonal directions. Figure 6i shows the generation and manipulation of Cherenkov surface plasmon wakes with a 1D array of aperture antennas.[176] The Cherenkov surface plasmon wakes were generated by creating a running wave of polarization along the nanostructure array that propagates faster than the SPP phase velocity.

4. Advanced Information Photonics

With the development of modern information photonics, optical devices with large information storage capacities are required. Metasurfaces for basic applications cannot accommodate this requirement. Thus, more complex metadevices with enhanced information storage capacities and multifunctionalities have been proposed. In this section, we discuss three types of metasurfaces involved with information photonics: metaholograms, coding metasurfaces, and multifunctional shared-aperture metasurfaces. Metaholograms are designed to store and release information with a higher resolution than their conventional counterparts. Coding metasurfaces provide a link between the physical world of metasurfaces and the digital and information world, and multifunctional metasurfaces can accommodate multiplexed information.

4.1. Metaholograms

Holography was first invented by Gabor in 1948 with the original intent of improving the resolution of electron microscopes.[177] Due to its significant capabilities of wavefront shaping and optical recording/reconstruction, numerous applications, such as data storage and information encryption, have follows. Traditional amplitude holograms rely on recording the interference patterns from the light scattered by an object and a coherent reference beam. The low conversion efficiency, due to much of the incident power being scattered or reflected in this classic approach, limits the practical applications. By translating the intensity of the interference patterns into phase variations, phase holograms provide a relatively high diffraction efficiency and can substantially increase the brightness of the reconstructed images;[178] additionally, with the use of CGHs in the past decade,[179,180] the required phase and amplitude distributions can be numerically calculated and then encoded into spatial light modulators (SLMs).[181] The smallest achievable hologram pixel size of conventional SLMs is on the order of a micrometer, which is several times the wavelength of visible light; their intrinsic limitations, such as higher-order diffraction and twin-image issues, are still challenging to avoid. Although a smaller pixel size can be achieved with advanced nanofabrication technologies, the high cost remains a limitation. Therefore, subwavelength metasurfaces have become a natural candidate for high resolution and efficient holography. Since the basic application of holograms is to record and reconstruct objects, we classify the metaholograms in an intuitive way: as single-color metaholograms and multicolor metaholograms.

4.1.1. Single-Color Metaholograms

This type of metaholograms cannot present different colors in one image because each pixel consists of one or several same unit cells. For the resonant phase metasurfaces, the response of phase and amplitude of each unit cell is dispersive; thus, only illumination with specific wavelengths can reconstruct metaholograms. For the P–B phase metasurfaces, with the broad bandwidth resonance and nondispersive phase response, the images can be rendered with various colors depending on the illuminating wavelengths.

Using V-shaped nanoapertures, a holographic image in the visible wavelength range has been reconstructed with a high resolution but low efficiency of 10%, as shown in **Figure 7**a.[182]

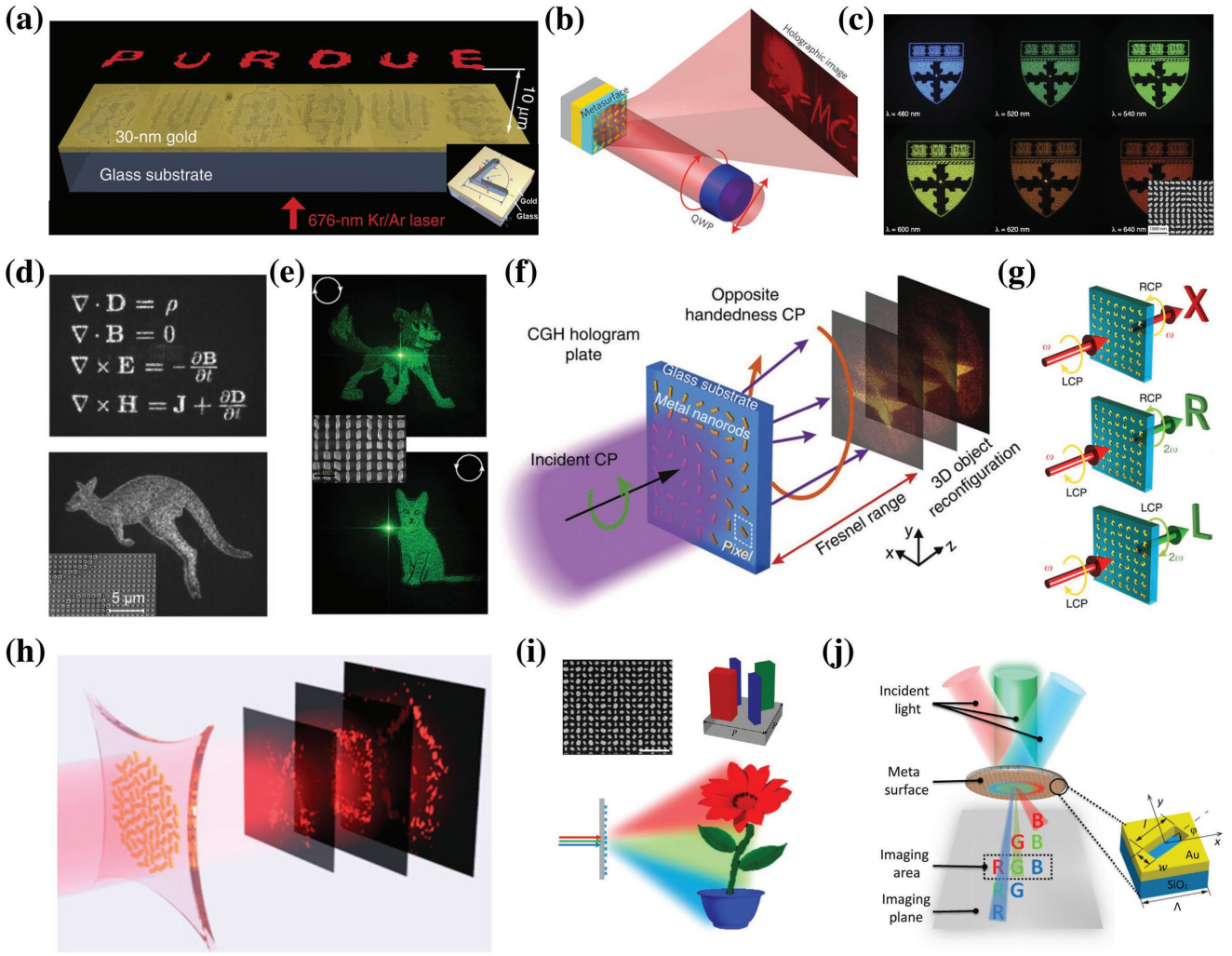

Figure 7. Metaholograms realized using metasurfaces. a) Measured holographic images reconstructed by a metasurface consisting of V-shaped nanoapertures under linearly polarized light. Inset: schematic view of the unit cell of the metasurface. Reproduced with permission.[182] Copyright 2013, Nature Publishing Group. b) Schematic illustration of the highly efficient reflection-type metahologram based on the combination of the P–B phase and MIM structures. Reproduced with permission.[49] Copyright 2015, Nature Publishing Group. c) Measured holographic images covering the visible spectrum reconstructed by a metasurface of titanium oxide. Inset: SEM image of the fabricated metasurface.[184] Copyright 2016, National Academy of Sciences. d) Experiment results of high-transmission and high-diffraction-efficiency holographic images recorded using a dielectric Huygens' metasurface. Inset: SEM image of the fabricated metasurface. Reproduced with permission.[185] Copyright 2016, Optical Society of America. e) Experiment results of polarization-switchable chiral metaholograms based on the combination of the P–B phase and the propagation phase. Inset: SEM image of the fabricated metasurface. Reproduced with permission.[192] Copyright 2017, American Physical Society. f) Schematic illustration of the 3D metahologram. Reproduced with permission.[193] Copyright 2013, Nature Publishing Group. g) Schematic illustration of the spin- and wavelength-multiplexed nonlinear metaholograms. Reproduced with permission.[196] Copyright 2016, Nature Publishing Group. h) Schematic illustration of a multiplexed metahologram on a stretchable substrate. Reproduced with permission.[197] Copyright 2017, American Chemical Society. i) Schematic illustration of multicolor dielectric metaholograms consisting of three types of silicon nanoblocks. Insets: SEM images of the fabricated metasurface and one meta-molecule consisting of four Si nanoblocks. Reproduced with permission.[200] Copyright 2016, American Chemical Society. j) Schematic illustration of an angle-sensitive multicolor metahologram with a single type of nanostructure pixel. Inset: Schematic view of the unit cell of the metasurface. Reproduced with permission.[203] Copyright 2016, American Association for the Advancement of Science.

One way to address the low efficiency is to adopt the MIM reflection configuration; with the combination of P–B phase and the MIM reflection configuration, a reflective-phase-only metahologram with a broadband spectral response in the visible/NIR range, a maximum efficiency of 80% has been presented, as illustrated in Figure 7b.[49] Similarly, combining the reflective operating mode with resonant phase metasurfaces has achieved a 50% efficiency in the NIR range; additionally, high-fidelity metaholograms were simultaneously projected at angles of 45° and 20° with respect to the impinging light.[183] Another approach to increase the efficiency of transmission-type metaholograms is to use high-contrast dielectrics or Huygens' metasurfaces. The P–B phase based on a high contrast metahologram made of titanium oxide has been used to provide a broadband high efficiency of ≈80% in the visible spectrum as presented in Figure 7c.[184] Eliminating the reflection using a Huygens'

metahologram has been experimentally demonstrated to generate grayscale high-resolution metaholograms that transmit over 90% and have a highest diffraction efficiency of over 99% in the NIR range, as shown in Figure 7d.[185] Inspired by this fact, a polarization-insensitive metahologram based on Huygens' metasurfaces with a 40% imaging efficiency at an NIR frequency[32] and a metahologram that functions at a shorter wavelength in the NIR range have been proposed.[186]

Higher-complexity polarization-multiplexed metaholograms that can reconstruct different holograms with different incident polarizations have also been demonstrated. A metahologram that can generate switchable dual images by controlling the incident polarization state based on the reflective resonant phase configuration for a visible wavelength was presented.[187] P–B phase-based metaholograms exhibiting multiple recording channels and helicity-dependent phase profiles that can integrate different multiplexing strategies into a single metahologram, such as polarization, position, and angle, have also been demonstrated in both the visible[188] and NIR range.[66,189] Broadband polarization-multiplexed metaholograms that operate throughout the visible and NIR range and are associated with the traditional detour phase have been presented under both circular[190] and linear polarization incidences.[191] Another recent notable method is the combination of the P–B phase and the propagation phase; two independent phase profiles can be imposed on any pair of orthogonal polarization states, resulting in chiral metaholograms characterized by fully independent far fields for each circular polarization, as presented in Figure 7e.[192]

Metaholograms with large information capacities have also been presented. 3D or multiplane metaholograms working in the visible and NIR range with position multiplexing (Figure 7f)[193] and both position and polarization multiplexing capacities were experimentally demonstrated.[194] Angle-multiplexed metaholograms were also proposed by encoding holographic information associated with various incident angles in a single metasurface; a dynamic holographic display was reconstructed by controlling the incident angle.[195]

New types of metaholograms have also been developed in recent years. Nonlinear metaholograms were realized using the P–B phase operating in both the linear and nonlinear regimes; different spin and wavelength multiplexed phase responses are associated with the same rotating nanoantenna, resulting in the reconstruction of multiple metaholograms generated independently by the fundamental and second harmonic generation waves with different spins, as indicated in Figure 7g.[196] A two-layer nonlinear metahologram was also created using a separate phase hologram embedded in each metasurface layer to yield the desired holographic images for the vertical or horizontal linear incident polarization.[37] Relative to linear metaholograms, the nonlinear metaholograms that function in the nonlinear regimes remove background noise at the fundamental frequency and provide additional multiplexing channels. By fabricating gold nanorods on a stretchable polydimethylsiloxane substrate, multiple distinct holographic images can be switchably displayed, as illustrated in Figure 7h.[197] A coding-metasurface-based reprogrammable metahologram was recently exploited; the digital state of each coding unit cell could be switched by electrically controlling the loaded diodes, resulting in different target holographic images that were realized by a single coding metasurface in real time.[198]

4.1.2. MultiColor Metaholograms

Distinct from single-color metaholograms, multicolor metaholograms can simultaneously achieve multiple images with different colors. The basic approach is to combine several narrow-band resonant nanostructures that are resonant at completely different wavelengths to form a super unit cell. Angle-sensitive multicolor metaholograms have also been developed to achieve a higher metahologram quality with a higher resolution and lower crosstalk among different colors.

Multicolor metaholograms could be presented based on the super unit cell design, with the combination of both the resonant[199] phase and the P–B phase (Figure 7i).[200,201] However, the super unit cell design inevitably increases the pixel size and may suffer from crosstalk among different colors; a novel angle-sensitive methodology has been proposed to achieve multicolor metaholograms with a single type of nanostructure pixel, as shown in Figure 7j,[202,203] by superimposing multiple holograms that were calculated separately for various color components and encoded with an additional phase shift for each color. In the reconstruction process, the illumination of three-primary-color lasers with a variety of tilted incident angles were used to decode different components to generate the desired multicolor images. Graphene oxides can also be used to generate wide-angle and multicolor 3D holograms through an athermal photoreduction process induced by a single femtosecond pulse.[204]

4.2. Coding Metasurfaces

Coding metasurfaces were proposed in 2014. Instead of using effective medium parameters, digital coding unit cells with specified phase responses can be used to characterize metasurfaces, as illustrated in **Figure 8**a.[205] The coding representation of a metasurface not only simplifies the design and optimization procedures of metasurfaces due to the digitalization of the unit cell geometry but also provides a link between the physical world and the digital world. Distinct from conventional metasurfaces, the design procedures and the functionalities of metasurfaces are determined by coding sequences, which represent different digital states of each coding unit cell. Furthermore, the coding sequences make coding metasurfaces able to be implemented by digital logic devices; thus, by changing the input coding sequences, different functionalities can be achieved in real time. By arranging coding unit cells with optimized coding sequences, the coding metasurfaces can be used to manipulate EM waves in a simpler and more efficient way.

4.2.1. Basic Coding Metasurfaces

The concept of coding metasurfaces was initially proposed and experimentally demonstrated in the microwave frequency due to the relative ease of fabrication and characterization.[205] For the initial 1-bit coding, binary digits "0" and "1" with EM phases of 0 and π were used to control the behaviors using different sequences of "0" and "1." A more complex multibit can be realized by introducing more discrete phases. One of the prominent advantages of a coding metasurface is that the

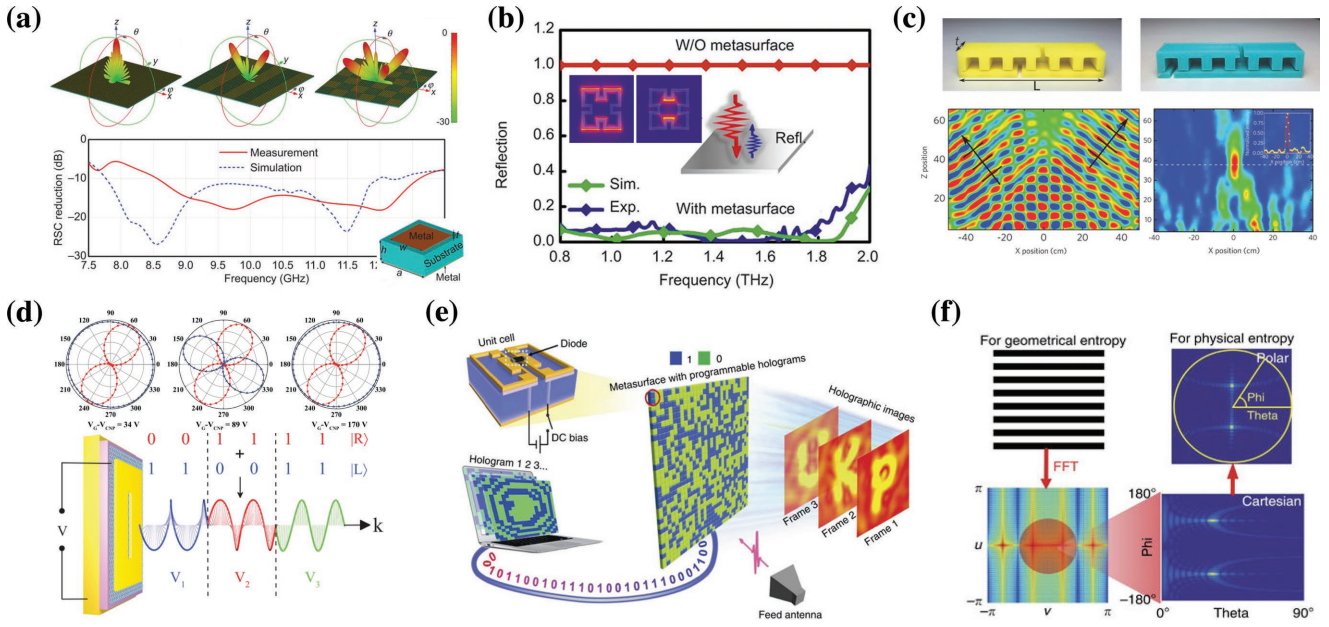

Figure 8. Various functionalities realized by coding metasurfaces. a) Simulation results of coding metasurfaces with various coding sequences (upper panel), simulation and measurement results of monostatic RCS reductions of a 1-bit coding metasurface (lower panel). Inset: schematic view of the unit cell of the coding metasurface. Reproduced with permission.[205] Copyright 2014, Nature Publishing Group. b) Measured and simulated backward scattering coefficients of a 2-bit metasurface in the THz range under normal incidence. Inset: simulated results of the Minkowski coding particle at different frequencies. Reproduced with permission.[206] Copyright 2015, Nature Publishing Group. c) Photograph of the fabricated "0" and "1" coding elements (upper panel), experimental acoustic temporal field distribution of the transmitted wave for normal incidence and a flat Fresnel lens based on 1-bit acoustic coding metasurfaces (lower panel). Reproduced with permission.[211] Copyright 2016, John Wiley and Sons. d) Simulated polarization state in the plane perpendicular to the wave vector for various gate voltages (upper panel) and schematic illustration of the polarization-division multiplexing technique using the proposed metadevice with a circular orthogonal polarization basis according to the superposition principle of polarization states (lower panel). Reproduced with permission.[215] Copyright 2016, John Wiley and Sons. e) Schematic illustration of EM reprogrammable metaholograms using a 1-bit coding metausrface. Inset: schematic view of the unit cell of the coding metasurface. Reproduced with permission.[198] Copyright 2017, Nature Publishing Group. f) Schematic of the processes used to calculate the physical entropy of a coding metasurface from its far-field pattern. Reproduced with permission.[217] Copyright 2016, Nature Publishing Group.

manipulation to EM waves can be achieved simply by changing the coding sequence, which determines how the coding unit cells with various digital states are arranged on a 2D plane. As another important application, radar cross-sections (RCSs) of metallic objects can also be reduced using both 1-bit and 2-bit coding metasurfaces with random coding patterns. The coding metasurfaces were extended to THz frequencies to realize broadband and wide-angle diffusion using multibit coding unit cells based on a Minkowski closed-loop, as shown in Figure 8b[206] and anomalous reflections with ring-shaped unit cells.[207] Based on the orthogonality of different frequencies, a frequency-dependent dual-functional coding metasurface in the THz range that can accomplish two independent functionalities at two designed frequencies was developed.[208] Using a specific design, a THz wave can be focused in the near-field region to generate a nondiffraction Bessel beam with an improved-transmittance triple-layered free-standing structure.[209] Because of the aforementioned isotropic geometric structures of the coding unit cell design, a fixed coding metasurface can have only one function, which is unrelated to the polarization of the incidence. The concept of coding metasurfaces has been extended from isotropic to anisotropic based on the different responses under perpendicularly polarized EM waves of anisotropic designs, resulting in polarization-controlled anisotropic coding metasurfaces.[210] The concept of coding metasurfaces has been exploited even in the acoustic regime by adopting 1-bit acoustic coding metasurfaces, as presented in Figure 8c; the functionalities of beam splitting and more complex Fresnel zone plates have been designed and experimentally demonstrated.[211] A Fresnel plate incorporating an acoustic coding metasurface can operate over a certain bandwidth due to the broadband feature of the designed unit cell. Using the same design, multiband ultrathin asymmetric transmission of an acoustic wave was proposed by breaking the spatial inversion symmetry based on the constructive and destructive interferences of acoustic-wave coupling between the coded elements; using this configuration, the effect of asymmetric transmission can be easily switched on and off by changing the coding patterns.[212]

4.2.2. Programmable Coding Metasurfaces

In previous discussions, various unit cells were used to characterize different coding states; to truly link the physical world to the digital world using coding metasurfaces, however, a variety of coding states should be realized by a single unit cell. For this purpose, an elaborately designed structure was proposed to achieve a real digital coding unit cell.[205] A pin-diode was mounted between two separated metallic structures on the top-side of the dielectric substrate, which was controlled using the

DC voltage. The reflection phase difference reached π when the diode was biased "on" and "off" so that the digital states "0" and "1" of the coding metasurfaces could be electrically controlled by the pin-diode using a DC voltage. Thus, a single coding metasurface was composed of designed unit cells featuring numerous functions with various coding-sequence possibilities. When all possible coding sequences are stored in a field programmable gate array (FPGA), a variety of functionality can be dynamically generated in a programmable way. Taking advantages of the dynamically controlled programmable coding metasurfaces, a transmission-type 2-bit programmable coding metasurface in the microwave frequency for single-antenna and single-frequency imaging was developed.[213] When an FPGA inputs a series of random coding sequences into the programmable metasurface, multiple independently random radiation patterns are generated, illuminating the object to be imaged. For large-scale imaging problems, a compressed-sensing technique based on a programmable coding metasurface system was experimentally validated for high-resolution microwave imaging with excellent performance.[214] A metadevice composed of a metallic metasurface and graphene that can dynamically modulate the polarization state of a reflective wave with a wide tunable range in the MIR range was proposed, as illustrated in Figure 8d.[215] In this device, the phase retardation difference between the two orthogonal *E*-field components caused by the metadevice is controlled using a switching gate voltage applied on the graphene at one of three different values, and the incident linearly polarized light is dynamically converted into LCP light, RCP light, or linearly cross-polarized light in the reflection direction. Additionally, the programmable metasurfaces can be used to produce programmable hologram imaging, resulting in a variety of target holographic images realized in real time using a single coding metasurface, as indicated in Figure 8e.[198]

4.2.3. Information Operations with Coding Metasurfaces

Information entropy was originally used to measure the unpredictability of an information state, or equivalently, of the average value of an information source.[216] The larger the entropy, the more uncertainty the information source has and the more information it carries. As a link between the physical world and the digital world, a method of measuring the information carried by coding metasurfaces was recently proposed using information entropy, as shown in Figure 8f.[217] An approximately proportional relationship was found between the geometrical and physical entropies by calculating them for a series of coding patterns, which means that the information of the radiated pattern can be controlled by modulating the corresponding coding pattern with a certain geometrical entropy. Inspired by the convolution theorem in Fourier transforms, a new coding strategy called the scattering pattern shift was proposed that can rotate the scattering pattern to a target direction with little distortion and realize beam scanning with a continuous scanning angle.[218] Based on the principle of scattering pattern shift, ring-shaped scattering patterns with controllable shapes and directions were generated by arranging the gradient coding sequence that varies along the radial direction.[219] Another application is a controllable random metasurface that can control the probability of random scatterings appearing in certain directions by combining a random coding pattern with an additional gradient coding pattern.[220]

4.3. Multifunctional Shared-Aperture Metasurfaces

Most metasurfaces that we have already discussed were designed to realize a single functionality. With the development of modern photonics, ultracompact, multifunctional, and integrated optical devices are desired that can control the phase, amplitude and polarization independently. Inspired by the concept of shared-aperture antennas,[221] which were originally used for steering radar beams, this critical need has been addressed by demonstrating multifunctional metasurfaces.[222,223] The antennas use a single common aperture to simultaneously perform multiple functionalities. Three approaches were proposed for the realization of multifunctional shared-aperture metasurfaces: segmentation, interleaving, and harmonic responses, as illustrated in **Figure 9**a. The segmentation approach suffers from a low angular resolution and high noise. The interleaving approach suffers from speckle noise and is hindered by capacity reduction; however, this approach offers high flexibility in multifunctionalities generation. In contrast, the harmonic response concept constitutes a suitable platform to realize an accurate angularly resolved multibeam possessing negligible noise and a high information capacity; however, this approach restricts design flexibility. Relative to the segmentation approach, interleaved and harmonic response metasurfaces are potential candidates for realizing on-demand, multifunctional on-chip photonics. Additionally, a momentum analytical method was proposed to provide a generalized approach for designing multifunctional metasurfaces.[224]

4.3.1. Segmented Metasurfaces

In the segmentation approach, the aperture is spatially divided into separated subarrays imprinted using various phase functions. As a result of this division, a reduction of the angular resolution is inevitable. An ultrathin flat lens that can generate multiple focal points along the longitudinal direction was realized by applying this concept. Unlike conventional multifoci diffractive lenses, multiple focal points with different focal lengths can be achieved by changing the polarization state of the incident light.[225] Moreover, by adding the phase arrays of optical vortices into this multifoci design, a nanostructured focusing optical vortex generator with multiple focal planes is enabled, as shown in Figure 9b.[226] By designing each segmentation to function as an efficient polarization splitter for one of the different polarization states, chip-size plasmonic spectropolarimeters were demonstrated, as indicated in Figure 9c.[99] The spectropolarimeters can diffract normally incident light in six predesigned directions whose polar angles are proportional to the wavelengths, and the contrast in the corresponding diffraction intensities provides a direct measure of the incident polarization state through the retrieval of the associated Stokes parameters. Another layout aim is to individually design each segmentation to function for

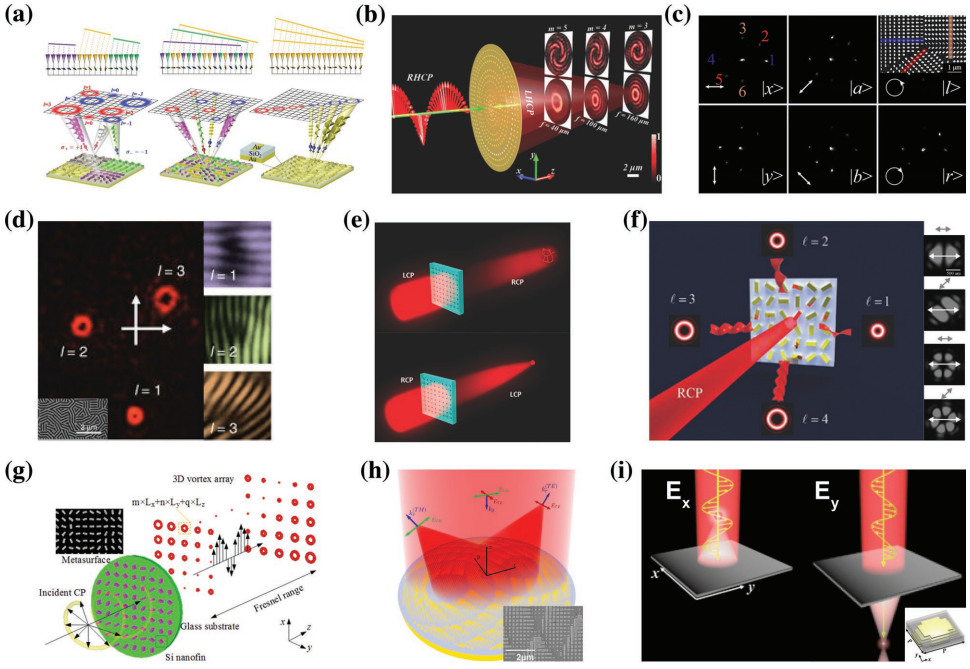

Figure 9. Multifunctional shared-aperture metasurfaces. a) Schematics of 1D phased arrays and far-field intensity distribution of wavefronts with positive (red) and negative (blue) helicities emerging from segmented, interleaved, and harmonic-response metasurfaces. Reproduced with permission.[222] Copyright 2016, American Association for the Advancement of Science. b) Schematic and measured results of the nanostructured focusing optical vortex generator with multiple focal planes. Reproduced with permission.[226] Copyright 2016, John Wiley and Sons. c) Measured far-field images of the diffraction spots for six different incident state of polarizations, each resulting in a unique intensity distribution. Inset: SEM image of fabricated metasurface. Reproduced with permission.[99] Copyright 2017, American Chemical Society. d) Experimental realization of multichannel optical vortices and verification of the desired topological charges. Inset: SEM image of fabricated metasurface. Reproduced with permission.[229] Copyright 2017, Nature Publishing Group. e) Schematic of the polarization-selective dual-functional metasurface, a metahologram and a lens could be achieved depending on the helicity of the incident light. Reproduced with permission.[232] Copyright 2016, John Wiley and Sons. f) Schematic of off-axis multi-OAM generation and experimentally observed superpositions of OAM states. Reproduced with permission.[236] Copyright 2017, John Wiley and Sons. g) Illustration of the generation and reconstruction procedure of a 3D vortex array based on a dielectric metasurface. Inset: SEM image of fabricated metasurface. Reproduced with permission.[237] Copyright 2017, American Chemical Society. h) Illustration of the polarization-controlled polarization splitting and focusing multifunction metamirror. Inset: SEM image of fabricated metasurface. Reproduced with permission.[240] Copyright 2017, American Chemical Society. i) Schematic illustration of the polarization-dependent full-space bifunctional metadevices. Inset: schematic view of the unit cell of the metasurface. Reproduced with permission.[242] Copyright 2017, American Physical Society.

a single wavelength; thus, wavelength-multiplexed multifunctional metasurfaces can be achieved. Based on this logic, achromatic lenses have been exploited via setting each segmentation to have the same focal length.[126,227]

4.3.2. Interleaved Metasurfaces

To enhance the angular resolution, an interleaved approach can be applied, in which multiple desired phase profiles are interleaved within the entire aperture.[228] Each phase profile is associated with a different subarray and is subjected to a thinning process to achieve a sufficient bandwidth, an adequate signal-to-noise ratio (SNR) and the desired functionalities. Although the stochastic thinning process still affects the SNR of the radiation profile, which causes this approach to suffer from speckle noise, the high flexibility in multifunctionality generation makes interleaved metasurfaces attractive and practical. Multichannel optical vortices and vectorial vortices have been proposed to extend the extraordinary information capacity and the polarization helicity control in the geometric phase mechanism, which is implemented in a straightforward manner using 2D structures by imprinting optical antenna patterns, as shown in Figure 9d.[228,229] By substituting metaholograms for some of the optical vortices, metaholograms and the superposition of optical vortices in multiple channels can be realized simultaneously.[230] By continuously changing the helicity of the incident light, polarization-dependent holographic images in two channels along the horizontal direction and the continuous control of the OAM superposition in two channels along the vertical direction were realized. Another helicity-dependent strategy was proposed to integrate two distinct functionalities by designing two functionalities that operated separately in the positive and negative sides of the metasurfaces. An interleaved metasurface can function either as a spherical or cylindrical lens[231] or as a metahologram and a lens (Figure 9e)[232] depending on the helicity of the incident light. Although this straightforward approach produces background noise, which decreases the SNR of the generated functionalities, such noise can be deceased by optimization methods, such as the angle-multiplexing method. As mentioned in the preceding section, wavelength-multiplexed interleaved metasurfaces have been exploited in this way.

Multifunctional metasurface lenses have been created by interleaving multiple distinct optical elements. multifunctional

wavefront shaping can be accomplished within a single shared aperture without reducing the NA of each subelement.[233] Multicolor imaging with a high spatial resolution and optical imaging functionality with simultaneous color separation have been obtained using this design. Achromatic lenses[71,125,227] and multicolor metaholograms,[199–201] as previously discussed, have also been exploited based on interleaved metasurfaces.

4.3.3. Harmonic-Response Metasurfaces

To improve the SNR, a harmonic response approach can be adopted in which the harmonic orders of the phase function are exploited to produce multiple wavefronts, resulting in negligible noise and a high information capacity. Thus, high-capacity optical communication can be achieved by combining harmonic-response metasurfaces with OAM-carrying optical vortices. To focus the intensity of the generated optical vortex, metasurfaces integrated with a lens and an optical vortex generator have been explored.[226,234] By imposing the phase profile of a linear gradient and an optical vortex, a converted vortex beam with a high purity can be separated from the unconverted and other undesirable beam components in a specifically designed diffraction angle.[143] Multichannel optical vortices with both phase and amplitude modulation have also been demonstrated.[235] Higher-complexity continuously polarization-controlled OAM superpositions in multiple channels have also been proposed, as presented in Figure 9f.[236] Arbitrary manipulation of OAM superpositions in four channels was achieved by controlling the helicity of the incident light. To further enhance the information capacity, a 3D volumetric vortex array with independently controllable topological charges of a sequence of coaxial beam profiles in the longitudinal propagation direction that can be present for the 2D diffraction orders in each transverse plane was recently explored, as illustrated in Figure 9g.[237] In addition to multichannel optical vortices generators, multiple optical vortices multiplexers and demultiplexers based on a highly integrated off-axis technique have been presented.[238] As a multiplexer, beams without OAM can be transferred into coaxial beams carrying various OAM features using various incident angles; as a demultiplexer, coaxial beams carrying multi-OAMs can be divided into various directions with fundamental modes. Large-angle metasurface deflectors to steer incident NIR plane waves to various diffraction orders according to the wavelengths with a high average efficiency for each wavelength using an iterative optimization solver have been produced.[239] Polarization-controlled optical metadevices have been developed based on harmonic-response metasurfaces as well, such as a polarization splitting and focusing metamirror that can simultaneously split orthogonal light polarizations and focus them into different focal spots, as shown in Figure 9h.[240] Bifunctional metadevices composed of anisotropic unit cells with polarization-dependent transmission and reflection phase responses to efficiently manipulate EM waves in the full space in the microwave regime were recently proposed, as illustrated in Figure 9i.[241,242] Relying on different optimization methods, the harmonic response concept can also be implemented in multi-image metaholograms, as we discussed in Section 4.1.[188,189,192–195,197,202,203]

5. Conclusions and Outlook

Phase gradient metasurfaces enable us to create an arbitrary phase profile for wavefront control and beam forming with a subwavelength resolution. We have summarized various methods that have been proposed to realize phase control and divide the phase into three types according to their generation mechanisms and features, which can be implemented using both metallic and dielectric nanostructures. Additionally, we have reviewed various applications based on phase gradient metasurfaces. This area is an emerging, promising and rapidly developing research domain that is attracting increasing interest from researchers. Many novel applications have been proposed, and many new branches have appeared in this field in the past few years. Among them, we wish to emphasize certain promising areas that may greatly broaden the scope of application of phase gradient metasurfaces:

(1) *Waveguide-based metasurfaces*: Optical waveguides play an important role in the transfer of energy and signals in integrated optical circuit systems. Metamaterials have great potential for controlling the propagation of light in a waveguide.[242–248] With a metasurface, vertical incidence light can couple into the waveguide,[249] and the waveguide can act as an in-plane polarimeter.[250] The effective relative permeability of the waveguide can also be controlled using split-ring resonators.[251] Recently, it was reported that phase gradient metasurfaces can be integrated into waveguides to realize mode conversion, polarization rotation and asymmetric optical power transmission.[252] By introducing a phase gradient along the propagation direction of light with plasmonic or dielectric nanoantennas, an effective wavevector can be imparted to the incident mode, which can convert the higher-order waveguide mode into a lower-order mode or an SW. The effective wavevector introduced by the nanoantenna arrays can also be used to relax the phase-matching requirement in on-chip nonlinear wavelength conversion.[253] Notably, an optical fiber, as another type of waveguide, can also be an important platform to implement phase gradient metasurfaces. By integrating a phase gradient metasurface on an optical fiber tip, optical fiber "metatips" that can steer a beam in the NIR region have been proposed and experimentally realized.[254] In view of the extensive applications of waveguides and the powerful light modulation abilities of phase gradient metasurfaces, waveguide-based metasurfaces are expected to be a promising field in future integrated optical circuits and optical communication systems.

(2) *Dynamically reconfigurable metasurfaces*: Dynamically reconfigurable metasurfaces are highly desirable for the realization of advanced optical devices and can greatly enhance the abilities of EM wave controls. However, most of the currently proposed phase gradient metasurfaces are static, which means that their functions cannot be changed or tuned once the design is completed. Currently, several methods have been proposed to realize dynamically reconfigurable metasurfaces,[255] such as electrical control,[55,153,215,256,257] optical control,[121,258–260] mechanical control,[119,120] and thermal control.[261,262] Dynamical phase gradient metasurfaces are often implemented using active functional materials. For

example, tunable infrared anomalous refraction[55] and optical polarization encoding[215] by varying the Fermi energy of graphene have been proposed. The refractive index of GST can be changed by changing the GST structural phase form amorphous to crystalline. Based on this property, several phase gradient metasurfaces have been realized from the MIR region[134] to the NIR[260,263,264] and the visible regions.[121] Recently, Qiu et al. proposed a reconfigurable active metalens at microwave frequencies that can simultaneously control multiple focal spots. However, realizing real-time wavefront control that can individually modulate every phase shifter element from 0 to 2π remains a considerable challenge, particularly for the short-wavelength region. Notably, a dynamic change of the phase gradient can lead to some new phenomena and enable so-called time-gradient metasurfaces,[266,267] which can break the photon energy conservation constraint and realize nonreciprocal propagation of light.

(3) *Gradient nonlinear metasurfaces*: Although the nonlinear P–B phase and the abrupt phase of metasurfaces can both cover the full 2π range, providing unprecedented control over the nonlinear generation process relative to conventional nonlinear optical crystals, the conversion efficiency of nonlinear metasurfaces is very low. Currently, weak signals can be detected only with highly sensitive cameras, which are applied in optical encryption.[268] Therefore, new materials and systems should be explored to enhance the conversion process. One strategy is to couple metasurfaces to the intersubband transitions of semiconductors.[58,269] Another strategy inspired by conventional quasi-phase-matching was recently proposed,[270] using multilayered nonlinear metasurfaces, the nonlinear conversion efficiency can be dramatically enhanced. With further developments in the enhancement of the conversion efficiency, an increasing number of nonlinear metadevices can open new avenues for data storage, optical information security and display.

(4) *Quantum metasurfaces*: The application scope of metasurfaces has extended from classical systems to quantum systems in recent years.[271–273] The capacities of metasurfaces for polarization and phase modulation provide a promising route for on-chip quantum state engineering. An anisotropic quantum vacuum can be realized using the polarization-dependent response of a metasurface that can act as a spherical mirror for one polarization state while simultaneously serving as a normal mirror for another polarization state.[272] As a result, a strong anisotropy in the decay rate of a quantum emitter located above the metasurface can be achieved. Such an artificial anisotropic quantum vacuum can induce remote quantum interference among radiative decay channels in a multilevel quantum emitter with orthogonal transitions. Metasurfaces can also be used to realize the quantum entanglement of qubits at the chip level. The metasurface-mediated quantum entanglement between two qubits separated by macroscopic distances with large values of concurrence has been theoretically demonstrated.[273] The interaction of the two qubits was mediated by a metasurface that can redirect the emission from the source qubit toward the target qubit. By combining the metasurface platform with quantum systems, quantum metasurfaces may find numerous applications in on-chip quantum science and technologies.

In summary, thanks to the flexible ability of phase control, the simplicity of fabrication and integration, the subwavelength resolution of the phase shifter elements, and the diversity of functions and other advantages, phase gradient metasurfaces are expected to play a significant role in the realization of future nanophotonic devices and to have other advanced applications.

Acknowledgements

This work was supported by the National Key Research and Development Program of China (2016YFA0301102 and 2017YFA0303800), the Natural Science Foundation of China (11774186, 11574163 and 61378006), the Natural Science Foundation of Tianjin (16JCQNJC01700), and 111 Project (B07013).

Conflict of Interest

The authors declare no conflict of interest.

Keywords

dielectric metasurfaces, flat optical elements, nonlinear metasurfaces, phase manipulation, plasmonic metasurfaces

Received: January 24, 2018
Revised: March 18, 2018
Published online:

[1] R. A. Shelby, D. R. Smith, S. Schultz, *Science* **2001**, *292*, 77.
[2] T. J. Yen, W. J. Padilla, N. Fang, D. C. Vier, D. R. Smith, J. B. Pendry, D. N. Basov, X. Zhang, *Science* **2004**, *303*, 1494.
[3] J. B. Pendry, D. Schurig, D. R. Smith, *Science* **2006**, *312*, 1780.
[4] N. Yu, P. Genevet, M. A. Kats, F. Aieta, J.-P. Tetienne, F. Capasso, Z. Gaburro, *Science* **2011**, *334*, 333.
[5] X. Ni, N. K. Emani, A. V. Kildishev, A. Boltasseva, V. M. Shalaev, *Science* **2012**, *335*, 427.
[6] N. Yu, F. Capasso, *Nat. Mater.* **2014**, *13*, 139.
[7] S. B. Glybovski, S. A. Tretyakov, P. A. Belov, Y. S. Kivshar, C. R. Simovski, *Phys. Rep.* **2016**, *634*, 1.
[8] H.-T. Chen, A. J. Taylor, N. Yu, *Rep. Prog. Phys.* **2016**, *79*, 076401.
[9] L. Zhang, S. Mei, K. Huang, C.-W. Qiu, *Adv. Opt. Mater.* **2016**, *4*, 818.
[10] H.-H. Hsiao, C. H. Chu, D. P. Tsai, *Small Methods* **2017**, *1*, 1600064.
[11] W. Wan, J. Gao, X. Yang, *Adv. Opt. Mater.* **2017**, *5*, 1700541.
[12] F. Ding, A. Pors, S. I. Bozhevolnyi, *Rep. Prog. Phys.* **2017**, *81*, 026401.
[13] M. A. Kats, N. Yu, P. Genevet, Z. Gaburro, F. Capasso, *Opt. Express* **2011**, *19*, 21748.
[14] D. J. Griffiths, *Introduction to Electrodynamics*, 3rd ed., Prentice Hall, Upper Saddle River, NJ **1999**.
[15] R. Blanchard, G. Aoust, P. Genevet, N. Yu, M. A. Kats, Z. Gaburro, F. Capasso, *Phys. Rev. B* **2012**, *85*, 155457.
[16] X. Ni, S. Ishii, A. V. Kildishev, V. M. Shalaev, *Light Sci. Appl.* **2013**, *2*, e72.
[17] F. Qin, L. Ding, L. Zhang, F. Monticone, C. C. Chum, J. Deng, S. Mei, Y. Li, J. Teng, M. Hong, S. Zhang, A. Alù, C.-W. Qiu, *Sci. Adv.* **2016**, *2*, e1501168.
[18] N. K. Grady, J. E. Heyes, D. R. Chowdhury, Y. Zeng, M. T. Reiten, A. K. Azad, A. J. Taylor, D. A. R. Dalvit, H.-T. Chen, *Science* **2013**, *340*, 1304.

[19] S. Sun, K.-Y. Yang, C.-M. Wang, T.-K. Juan, W. T. Chen, C. Y. Liao, Q. He, S. Xiao, W.-T. Kung, G.-Y. Gao, L. Zhou, D. P. Tsai, *Nano Lett.* **2012**, *12*, 6223.
[20] L. Zhang, J. Hao, M. Qiu, S. Zouhdi, J. K. W. Yang, C.-W. Qiu, *Nanoscale* **2014**, *6*, 12303.
[21] N. Liu, H. Guo, L. Fu, S. Kaiser, H, Schweizer , H. Giessen, *Adv. Mater.* **2007**, *19*, 3628.
[22] A. Pors, S. I. Bozhevolnyi, *Opt. Express* **2013**, *21*, 27438.
[23] C. Pfeiffer, A. Grbic, *Phys. Rev. Lett.* **2013**, *110*, 197401.
[24] C. Pfeiffer, N. K. Emani, A. M. Shaltout, A. Boltasseva, V. M. Shalaev, A. Grbic, *Nano Lett.* **2014**, *14*, 2491.
[25] F. Monticone, N. M. Estakhri, A. Alù, *Phys. Rev. Lett.* **2013**, *110*, 203903.
[26] J. C. Ginn, I. Brener, D. W. Peters, J. R. Wendt, J. O. Stevens, P. F. Hines, L. I. Basilio, L. K. Warne, J. F. Ihlefeld, P. G. Clem, M. B. Sinclair, *Phys. Rev. Lett.* **2012**, *108*, 097402.
[27] J. M. Geffrin, B. García-Cámara, R. Gómez-Medina, P. Albella, L. S. Froufe-Pérez, C. Eyraud, A. Litman, R. Vaillon, F. González, M. Nieto-Vesperinas, J. J. Sáenz, F. Moreno, *Nat. Commun.* **2012**, *3*, 1171.
[28] I. Staude, A. E. Miroshnichenko, M. Decker, N. T. Fofang, S. Liu, E. Gonzales, J. Dominguez, T. S. Luk, D. N. Neshev, I. Brener, Yu. S. Kivshar, *ACS Nano* **2013**, *7*, 7824.
[29] J. Cheng, D. Ansari-Oghol-Beig, H. Mosallaei, *Opt. Lett.* **2014**, *39*, 6285.
[30] M. Decker, I. Staude, M. Falkner, J. Dominguez, D. N. Neshev, I. Brener, T. Pertsch, Y. S. Kivshar, *Adv. Opt. Mater.* **2015**, *3*, 813.
[31] S. Campione, L. I. Basilio, L. K. Warne, M. B. Sinclair, *Opt. Express* **2015**, *23*, 2293.
[32] K. E. Chong, L. Wang, I. Staude, A. R. James, J. Dominguez, S. Liu, G. S. Subramania, M. Decker, D. N. Neshev, I. Brener, Y. S. Kivshar, *ACS Photonics* **2016**, *3*, 514.
[33] M. I. Shalaev, J. Sun, A. Tsukernik, A. Pandey, K. Nikolskiy, N. M. Litchinitser, *Nano Lett.* **2015**, *15*, 6261.
[34] K. E. Chong, I. Staude, A. James, J. Dominguez, S. Liu, S. Campione, G. S. Subramania, T. S. Luk, M. Decker, D. N. Neshev, I. Brener, Y. S. Kivshar, *Nano Lett.* **2015**, *15*, 5369.
[35] Y. F. Yu, A. Y. Zhu, R. Paniagua-Domínguez, Y. H. Fu, B. Luk'yanchuk, A. I. Kuznetsov, *Laser Photonics Rev.* **2015**, *9*, 412.
[36] E. Almeida, G. Shalem, Y. Prior, *Nat. Commun.* **2016**, *7*, 10367.
[37] E. Almeida, O. Bitton, Y. Prior, *Nat. Commun.* **2016**, *7*, 12533.
[38] S. Pancharatnam, *Proc. Indian Acad. Sci.* **1956**, *44*, 247.
[39] M. V. Berry, *J. Mod. Opt.* **1987**, *34*, 1401.
[40] Z. Bomzon, V. Kleiner, E. Hasman, *Opt. Lett.* **2001**, *26*, 1424.
[41] Z. Bomzon, G. Biener, V. Kleiner, E. Hasman, *Opt. Lett.* **2002**, *27*, 1141.
[42] E. Hasman, V. Kleiner, G. Biener, A. Niv, *Appl. Phys. Lett.* **2003**, *82*, 328.
[43] C. Menzel, C. Rockstuhl, F. Lederer, *Phys. Rev. A* **2010**, *82*, 053811.
[44] M. Kang, T. Feng, H.-T. Wang, J. Li, *Opt. Express* **2012**, *20*, 15882.
[45] L. Huang, X. Chen, H. Mühlenbernd, G. Li, B. Bai, Q. Tan, G. Jin, T. Zentgraf, S. Zhang, *Nano Lett.* **2012**, *12*, 5750.
[46] X. Ding, F. Monticone, K. Zhang, L. Zhang, D. Gao, S. N. Burokur, A. de Lustrac, Q. Wu, C.-W. Qiu, A. Alù, *Adv. Mater.* **2014**, *27*, 1195.
[47] L. Liu, X. Zhang, M. Kenney, X. Su, N. Xu, C. Ouyang, Y. Shi, J. Han, W. Zhang, S. Zhang, *Adv. Mater.* **2014**, *26*, 5031.
[48] S.-C. Jiang, X. Xiong, Y.-S. Hu, S.-W. Jiang, Y.-H. Hu, D.-H. Xu, R.-W. Peng, M. Wang, *Phys. Rev. B* **2015**, *91*, 125421.
[49] G. Zheng, H. Mühlenbernd, M. Kenney, G. Li, T. Zentgraf, S, Zhang , *Nat. Nanotechnol.* **2015**, *10*, 308.
[50] Z. Liu, Z. Li, Z. Liu, J. Li, H. Cheng, P. Yu, W. Liu, C. Tang, C. Gu, J. Li, S. Chen, J. Tian, *Adv. Funct. Mater.* **2015**, *25*, 5428.
[51] Z. Li, W. Liu, H. Cheng, J. Liu, S. Chen, J. Tian, *Sci. Rep.* **2016**, *6*, 35485.
[52] D. Lin, P. Fan, E. Hasman, M. L. Brongersma, *Science* **2014**, *345*, 298.
[53] M. Khorasaninejad, W. T. Chen, R. C. Devlin, J. Oh, A. Y. Zhu, F. Capasso, *Science* **2016**, *352*, 1190.
[54] M. Khorasaninejad, W. T. Chen, A. Y. Zhu, J. Oh, R. C. Devlin, D. Rousso, F. Capasso, *Nano Lett.* **2016**, *16*, 4595.
[55] H. Cheng, S. Chen, P. Yu, W. Liu, Z. Li, J. Li, B. Xie, J. Tian, *Adv. Opt. Mater.* **2015**, *3*, 1744.
[56] G. Li, S. Chen, N. Pholchai, B. Reineke, P. W. H. Wong, E. Y. B. Pun, K. W. Cheah, T. Zentgraf, S. Zhang, *Nat. Mater.* **2015**, *14*, 607.
[57] S. Chen, G. Li, F. Zeuner, W. H. Wong, E. Y. B. Pun, T. Zentgraf, K. W. Cheah, S. Zhang, *Phys. Rev. Lett.* **2014**, *113*, 033901.
[58] M. Tymchenko, J. S. Gomez-Diaz, J. Lee, N. Nookala, M. A. Belkin, A. Alù, *Phys. Rev. Lett.* **2015**, *115*, 207403.
[59] M. Khorasaninejad, F. Capasso, *Nano Lett.* **2015**, *15*, 6709.
[60] M. Khorasaninejad, A. Zhu, C. Roques-Carmes, W. T. Chen, J. Oh, I. Mishra, R. C. Devlin, F. Capasso, *Nano Lett.* **2016**, *16*, 7229.
[61] M. Khorasaninejad, F. Aieta, P. Kanhaiya, M. A. Kats, P. Genevet, D. Rousso, F. Capasso, *Nano Lett.* **2015**, *15*, 5358.
[62] F. Aieta, M. A. Kats, P. Genevet, F. Capasso, *Science* **2015**, *347*, 1342.
[63] E. Schonbrun, K. Seo, K. B. Crozier, *Nano Lett.* **2011**, *11*, 4299.
[64] P. Lalanne, S. Astilean, P. Chavel, E. Cambril, H. Launois, *J. Opt. Soc. Am. A* **1999**, *16*, 1143.
[65] S. Vo, D. Fattal, W. V. Sorin, Z. Peng, T. Tran, M. Fiorentino, R. G. Beausoleil, *IEEE Photonics Technol. Lett.* **2014**, *26*, 1375.
[66] A. Arbabi, Y. Horie, M. Bagheri, A. Faraon, *Nat. Nanotechnol.* **2015**, *10*, 937.
[67] Z. Guo, L. Zhu, F. Shen, H. Zhou, R. Gao, *RSC Adv.* **2017**, *7*, 9872.
[68] A. Arbabi, Y. Horie, A. J. Ball, M. Bagheri, A. Faraon, *Nat. Commun.* **2015**, *6*, 7069.
[69] H. Zuo, D.-Y. Choi, X. Gai, P. Ma, L. Xu, D. N. Neshev, B. Zhang, B. Luther-Davies, *Adv. Opt. Mater.* **2017**, *5*, 1700585.
[70] M. Khorasaninejad, Z. Shi, A. Y. Zhu, W. T. Chen, V. Sanjeev, A. Zaidi, F. Capasso, *Nano Lett.* **2017**, *17*, 1819.
[71] E. Arbabi, A. Arbabi, S. M. Kamali, Y. Horie, A. Faraon, *Optica* **2016**, *3*, 628.
[72] S. A. Maier, *Plasmonics: Fundamentals and Applications*, Springer, NY, USA **2007**.
[73] L. Verslegers, P. B. Catrysse, Z. Yu, J. S. White, E. S. Barnard, M. L. Brongersma, S. Fan, *Nano Lett.* **2009**, *9*, 235.
[74] S. Ishii, V. M. Shalaev, A. V. Kildishev, *Nano Lett.* **2013**, *13*, 159.
[75] J. Sun, X. Wang, T. Xu, Z. A. Kudyshev, A. N. Cartwright, N. M. Lichinitser, *Nano Lett.* **2014**, *14*, 2726.
[76] L. Lin, X. M. Goh, L. P. McGuinness, A. Roberts, *Nano Lett.* **2010**, *10*, 1936.
[77] J. Li, S. Chen, H. Yang, J. Li, P, Yu , H. Cheng, C. Gu, H.-T. Chen, J. Tian, *Adv. Funct. Mater.* **2015**, *25*, 704.
[78] P. Yu, S. Chen, J. Li, H. Cheng, Z. Li, W. Liu, B. Xie, Z. Liu, J. Tian, *Opt. Lett.* **2015**, *40*, 3229.
[79] J. Li, P. Yu, C. Tang, H. Cheng, J. Li, S. Chen, J. Tian, *Adv. Opt. Mater.* **2017**, *5*, 1700152.
[80] Z. Li, W. Liu, H. Cheng, S. Chen, J. Tian, *Adv. Opt. Mater.* **2017**, *5*, 1700413.
[81] X. Hu, X. Wei, *Opt. Express* **2017**, *25*, 15208.
[82] F. Aieta, P. Genevet, N. Yu, M. A. Kats, Z. Gaburro, F. Capasso, *Nano Lett.* **2012**, *12*, 1702.
[83] A. Pors, O. Albrektsen, I. P. Radko, S. I. Bozhevolnyi, *Sci. Rep.* **2013**, *3*, 2155.
[84] F. Ding, Z. Wang, S. He, V. M. Shalaev, A. V. Kildishev, *ACS Nano* **2015**, *9*, 4111.
[85] Z. Li, E. Palacios, S. Butun, K. Aydin, *Nano Lett.* **2015**, *15*, 1615.
[86] M. Khorasaninejad, K. B. Crozier, *Nat. Commun.* **2014**, *5*, 5386.
[87] M. Wei, Q. Xu, Q. Wang, X. Zhang, Y. Li, J. Gu, Z. Tian, X. Zhang, J. Han, W. Zhang, *Appl. Phys. Lett.* **2017**, *111*, 071101.
[88] S. L. Jia, X. Wan, D. Bao, Y. J. Zhao, T. J. Cui, *Laser Photonics Rev.* **2015**, *9*, 545.
[89] O. Hosten, P. Kwiat, *Science* **2008**, *319*, 787.
[90] X. Yin, Z. Ye, J. Rho, Y. Wang, X. Zhang, *Science* **2013**, *339*, 1405.

[91] W. Luo, S. Xiao, Q. He, S. Sun, L. Zhou, *Adv. Opt. Mater.* **2015**, *3*, 1102.
[92] X. Ling, X. Zhou, X. Yi, W. Shu, Y. Liu, S. Chen, H. Luo, S. Wen, D. Fan, *Light Sci. Appl.* **2015**, *4*, e290.
[93] A. Shaltout, J. Liu, A. Kildishev, V. Shalaev, *Optica* **2015**, *2*, 860.
[94] X.-G. Luo, M.-B. Pu, X. Li, X.-L. Ma, *Light Sci. Appl.* **2017**, *6*, e16276.
[95] D. Wen, F. Yue, S. Kumar, Y. Ma, M. Chen, X. Ren, P. E. Kremer, B. D. Gerardot, M. R. Taghizadeh, G. S. Buller, X. Chen, *Opt. Express* **2015**, *23*, 10272.
[96] A. Pors, M. G. Nielsen, S. I. Bozhevolnyi, *Optica* **2015**, *2*, 716.
[97] J. P. Balthasar Mueller, K. Leosson, F. Capasso, *Optica* **2016**, *3*, 42.
[98] W. T. Chen, P. Török, M. R. Foreman, C. Y. Liao, W. Y. Tsai, P. R. Wu, D. P. Tsai, *Nanotechnology* **2016**, *27*, 224002.
[99] F. Ding, A. Pors, Y. Chen, V. A. Zenin, S. I. Bozhevolnyi, *ACS Photonics* **2017**, *4*, 943.
[100] F. Aieta, P. Genevet, M. A. Kats, N. Yu, R. Blanchard, Z. Gaburro, F. Capasso, *Nano Lett.* **2012**, *12*, 4932.
[101] X. Chen, L. Huang, H. Mühlenbernd, G. Li, B. Bai, Q. Tan, G. Jin, C.-W. Qiu, S. Zhang, T. Zentgraf, *Nat. Commun.* **2012**, *3*, 1198.
[102] A. Pors, M. G. Nielsen, R. L. Eriksen, S. I. Bozhevolnyi, *Nano Lett.* **2013**, *13*, 829.
[103] X. Chen, L. Huang, H. Mühlenbernd, G. Li, B. Bai, Q. Tan, G. Jin, C.-W. Qiu, T. Zentgraf, S. Zhang, *Adv. Opt. Mater.* **2013**, *1*, 517.
[104] Z. Zhao, M. Pu, H. Gao, J. Jin, X. Li, X. Ma, Y. Wang, P. Gao, X. Luo, *Sci. Rep.* **2015**, *5*, 15781.
[105] A. Arbabi, A. Faraon, *Sci. Rep.* **2017**, *7*, 43722.
[106] M. Khorasaninejad, W. T. Chen, J. Oh, F. Capasso, *Nano Lett.* **2016**, *16*, 3732.
[107] M. Khorasaninejad, W. T. Chen, A. Y. Zhu, J. Oh, R. C. Devlin, C. Roques-Carmes, I. Mishra, F. Capasso, *IEEE J. Sel. Top. Quantum Electron.* **2017**, *23*, 4700216.
[108] A. Y. Zhu, W.-T. Chen, M. Khorasaninejad, J. Oh, A. Zaidi, I. Mishra, R. C. Devlin, F. Capasso, *APL Photonics* **2017**, *2*, 036103.
[109] D. Headland, E. Carrasco, S. Nirantar, W. Withayachumnankul, P. Gutruf, J. Schwarz, D. Abbott, M. Bhaskaran, S. Sriram, J. Perruisseau-Carrier, C. Fumeaux, *ACS Photonics* **2016**, *3*, 1019.
[110] P. R. West, J. L. Stewart, A. V. Kildishev, V. M. Shalaev, V. V. Shkunov, F. Strohkendl, Y. A. Zakharenkov, R. K. Dodds, R. Byren, *Opt. Express* **2014**, *22*, 26212.
[111] B. H. Chen, P. C. Wu, V.-C. Su, Y.-C. Lai, C. H. Chu, I. C. Lee, J.-W. Chen, Y. H. Chen, Y.-C. Lan, C.-H. Kuan, D. P. Tsai, *Nano Lett.* **2017**, *17*, 6345.
[112] W. T. Chen, A. Y. Zhu, M. Khorasaninejad, Z. Shi, V. Sanjeev, F. Capasso, *Nano Lett.* **2017**, *17*, 3188.
[113] Y. Bao, Q. Jiang, Y. Kang, X. Zhu, Z. Fang, *Light Sci. Appl.* **2017**, *6*, e17071.
[114] J. Ding, S. An, B. Zheng, H. Zhang, *Adv. Opt. Mater.* **2017**, *5*, 1700079.
[115] W. X. Jiang, S. Ge, T. Han, S. Zhang, M. Q. Mehmood, C.-W. Qiu, T. J. Cui, *Adv. Sci.* **2016**, *3*, 1600022.
[116] A. Arbabi, E. Arbabi, S. M. Kamali, Y. Horie, S. Han, A. Faraon, *Nat. Commun.* **2016**, *7*, 13682.
[117] B. Groever, W. T. Chen, F. Capasso, *Nano Lett.* **2017**, *17*, 4902.
[118] W. Liu, Z. Li, H. Cheng, C. Tang, J. Li, S. Zhang, S. Chen, J. Tian, *Adv. Mater.* **2018**, *30*, 1706368.
[119] H. S. Ee, R. Agarwal, *Nano Lett.* **2016**, *16*, 2818.
[120] S. M. Kamali, E. Arbabi, A. Arbabi, Y. Horie, A. Faraon, *Laser Photonics Rev.* **2016**, *10*, 1002.
[121] Q. Wang, E. T. F. Rogers, B. Gholipour, C.-M. Wang, G. Yuan, J. Teng, N. I. Zheludev, *Nat. Photonics* **2016**, *10*, 60.
[122] E. Arbabi, A. Arbabi, S. M. Kamali, Y. Horie, A. Faraon, *Optica* **2017**, *4*, 625.
[123] S. Wang, P. C. Wu, V.-C. Su, Y.-C. Lai, C. Hung Chu, J.-W. Chen, S.-H. Lu, J. Chen, B. Xu, C.-H. Kuan, T. Li, S. Zhu, D. P. Tsai, *Nat. Commun.* **2017**, *8*, 187.
[124] G. H. Yuan, E. T. Rogers, N. I. Zheludev, *Light Sci. Appl.* **2017**, *6*, e17036.
[125] J. Hu, C.-H. Liu, X. Ren, L. J. Lauhon, T. W. Odom, *ACS Nano* **2016**, *10*, 10275.
[126] O. Avayu, E. Almeida, Y. Prior, T. Ellenbogen, *Nat. Commun.* **2017**, *8*, 14992.
[127] N. Yu, F. Aieta, P. Genevet, M. A. Kats, Z. Gaburro, F. Capasso, *Nano Lett.* **2012**, *12*, 6328.
[128] P. C. Wu, W.-Y. Tsai, W. T. Chen, Y.-W. Huang, T.-Y. Chen, J.-W. Chen, C. Y. Liao, C. H. Chu, G. Sun, D. P. Tsai, *Nano Lett.* **2017**, *17*, 445.
[129] H. F. Ma, Y. Q. Liu, K. Luan, T. J. Cui, *Sci. Rep.* **2016**, *6*, 39390.
[130] Z. Liu, Z. Li, Z. Liu, H. Cheng, W. Liu, C. Tang, C. Gu, J. Li, H.-T. Chen, S. Chen, J. Tian, *ACS Photonics* **2017**, *4*, 2061.
[131] A. Shaltout, J. Liu, V. M. Shalaev, A. V. Kildishev, *Nano Lett.* **2014**, *14*, 4426.
[132] P. Yu, J. Li, C. Tang, H. Cheng, Z. Liu, Z. Li, Z. Liu, C. Gu, J. Li, S. Chen, J. Tian, *Light Sci. Appl.* **2016**, *5*, e16096.
[133] D. Wen, F. Yue, C. Zhang, X. Zang, H. Liu, W. Wang, X. Chen, *Appl. Phys. Lett.* **2017**, *111*, 023102.
[134] T. Li, L. Huang, J. Liu, Y. Wang, T. Zentgraf, *Opt. Express* **2017**, *25*, 4216.
[135] L. Allen, M. W. Beijersbergen, R. J. Spreeuw, J. P. Woerdman, *Phys. Rev. A* **1992**, *45*, 8185.
[136] M. Padgett, J. Courtial, L. Allen, *Phys. Today* **2004**, *57*, 35.
[137] P. Genevet, N. Yu, F. Aieta, J. Lin, M. A. Kats, R. Blanchard, M. O. Scully, Z. Gaburro, F. Capasso, *Appl. Phys. Lett.* **2012**, *100*, 013101.
[138] J. He, X. Wang, D. Hu, J. Ye, S. Feng, Q. Kan, Y. Zhang, *Opt. Express* **2013**, *21*, 20230.
[139] E. Karimi, S. A. Schulz, I. De Leon, H. Qassim, J. Upham, R. W. Boyd, *Light Sci. Appl.* **2014**, *3*, e167.
[140] F. Yue, D. Wen, J. Xin, B. D. Gerardot, J. Li, X. Chen, *ACS Photonics* **2016**, *3*, 1558.
[141] J. Jin, J. Luo, X. Zhang, H. Gao, X. Li, M. Pu, P. Gao, Z. Zhao, X. Luo, *Sci. Rep.* **2016**, *6*, 24286.
[142] F. Zhang, M. Pu, X. Li, P. Gao, X. Ma, J. Luo, H. Yu, X. Luo, *Adv. Funct. Mater.* **2017**, *27*, 1704295.
[143] J. Zeng, L. Li, X. Yang, J. Gao, *Nano Lett.* **2016**, *16*, 3101.
[144] S. Chen, Y. Cai, G. Li, S. Zhang, K. W. Cheah, *Laser Photonics Rev.* **2016**, *10*, 322.
[145] Y. Yang, W. Wang, P. Moitra, I. I. Kravchenko, D. P. Briggs, J. Valentine, *Nano Lett.* **2014**, *14*, 1394.
[146] A. Zhan, S. Colburn, R. Trivedi, T. K. Fryett, C. M. Dodson, A. Majumdar, *ACS Photonics* **2016**, *3*, 209.
[147] P. Georgi, C. Schlickriede, G. Li, S. Zhang, T. Zentgraf, *Optica* **2017**, *4*, 1000.
[148] R. C. Devlin, A. Ambrosio, N. A. Rubin, J. P. B. Mueller, F. Capasso, *Science* **2017**, *358*, 896.
[149] G. Li, L. Wu, K. F. Li, S. Chen, C. Schlickriede, Z. Xu, S. Huang, W. Li, Y. Liu, E. Y. B. Pun, T. Zentgraf, K. W. Cheah, Y. Luo, S. Zhang, *Nano Lett.* **2017**, *17*, 7974.
[150] S. Keren-Zur, O. Avayu, L. Michaeli, T. Ellenbogen, *ACS Photonics* **2016**, *3*, 117.
[151] N. Xi, Z. J. Wong, M. Mrejen, Y. Wang, X. Zhang, *Science* **2015**, *349*, 1310.
[152] J. Y. H. Teo, L. J. Wong, C. Molardi, P. Genevet, *Phys. Rev. A* **2016**, *94*, 023820.
[153] C. Huang, J. Yang, X. Wu, J. Song, M. Pu, C. Wang, X. Luo, *ACS Photonics* **2017**, https://doi.org/10.1021/acsphotonics.7b01114.
[154] Y. Yang, L. Jing, B. Zheng, R. Hao, W. Yin, E. Li, C. M. Soukoulis, H. Chen, *Adv. Mater.* **2016**, *28*, 6866.
[155] B. Orazbayev, N. M. Estakhri, A. Alù, M. Beruete, *Adv. Opt. Mater.* **2016**, *5*, 1600606.
[156] S. M. Kamali, A. Arbabi, E. Arbabi, Y. Horie, A. Faraon, *Nat. Commun.* **2016**, *7*, 11618.

[157] J. Durnin, J. J. MiceliJr., J. H. Eberly, *Phys. Rev. Lett.* **1987**, *58*, 1499.
[158] M. Pu, X. Li, X. Ma, Y. Wang, Z. Zhao, C. Wang, C. Hu, P. Gao, C. Huang, H. Ren, X. Li, F. Qin, J. Yang, M. Gu, M. Hong, X. Luo, *Sci. Adv.* **2015**, *1*, e1500396.
[159] W. T. Chen, M. Khorasaninejad, A. Y. Zhu, J. Oh, R. C. Devlin, A. Zaidi, F. Capasso, *Light Sci. Appl.* **2017**, *6*, e16259.
[160] C. Pfeiffer, A. Grbic, *Phys. Rev. Appl.* **2014**, *2*, 044012.
[161] M. V. Berry, N. L. Balazs, *Am. J. Phys.* **1979**, *47*, 264.
[162] G. A. Siviloglou, D. N. Christodoulides, *Opt. Lett.* **2007**, *32*, 979.
[163] G. A. Siviloglou, J. Broky, A. Dogariu, D. N. Christodoulides, *Phys. Rev. Lett.* **2007**, *99*, 213901.
[164] Z. Li, H. Cheng, Z. Liu, S. Chen, J. Tian, *Adv. Opt. Mater.* **2016**, *4*, 1230.
[165] E.-Y. Song, G.-Y. Lee, H. Park, K. Lee, J. Kim, J. Hong, H. Kim, B. Lee, *Adv. Opt. Mater.* **2017**, *5*, 1601028.
[166] L. Zhang, M. Zhang, H. Liang, *Adv. Opt. Mater.* **2017**, *5*, 1700486.
[167] A. Minovich, A. E. Klein, N. Janunts, T. Pertsch, D. N. Neshev, Y. S. Kivshar, *Phys. Rev. Lett.* **2011**, *107*, 116802.
[168] L. Li, T. Li, S. M. Wang, C. Zhang, S. N. Zhu, *Phys. Rev. Lett.* **2007**, *107*, 126804.
[169] S. Sun, Q. He, S. Xiao, Q. Xu, X. Li, L. Zhou, *Nat. Mater.* **2012**, *11*, 426.
[170] H. F. Ma, X. Shen, Q. Cheng, W. X. Jiang, T. J. Cui, *Laser Photonics Rev.* **2014**, *8*, 146.
[171] W. Sun, Q. He, S. Sun, L. Zhou. *Light Sci. Appl.* **2016**, *5*, e16003.
[172] P. Genevet, J. Lin, M. A. Kats, F. Capasso, *Nat. Commun.* **2012**, *3*, 1278.
[173] L. Huang, X. Chen, B. Bai, Q. Tan, G. Jin, T. Zentgraf, S. Zhang, *Light Sci. Appl.* **2013**, *2*, e70.
[174] Y. Gorodetski, A. Niv, V. Kleiner, E. Hasman, *Phys. Rev. Lett.* **2008**, *101*, 043903.
[175] A. Pors, M. G. Nielsen, T. Bernardin, J.-C. Weeber, S. I. Bozhevolnyi, *Light Sci. Appl.* **2014**, *3*, e197.
[176] P. Genevet, D. Wintz, A. Ambrosio, A. She, R. Blanchard, F. Capasso, *Nat. Nanotechnol.* **2015**, *10*, 804.
[177] D. Gabor, *Nature* **1948**, *161*, 117.
[178] W. T. Cathey, *Appl. Opt.* **1970**, *9*, 1478.
[179] L. B. Lesem, P. M. Hirsch, J. A. Jordan, *Commun. ACM* **1968**, *11*, 661.
[180] C. Slinger, C. Cameron, M. Stanley, *Computer* **2005**, *38*, 46.
[181] K. Huang, H. Gao, G. Cao, P. Shi, X. Zhang, Y. Li, *Appl. Opt.* **2012**, *51*, 5149.
[182] X. Ni, A. V. Kildishev, V. M. Shalaev, *Nat. Commun.* **2013**, *4*, 2807.
[183] Y. Yifat, M. Eitan, Z. Iluz, Y. Hanein, A. Boag, J. Scheuer, *Nano Lett.* **2014**, *14*, 2485.
[184] R. C. Devlin, M. Khorasaninejad, W. T. Chen, J. Oh, F. Capasso, *Proc. Natl. Acad. Sci. USA* **2016**, *113*, 10473.
[185] L. Wang, S. Kruk, H. Tang, T. Li, I. Kravchenko, D. N. Neshev, Y. S. Kivshar, *Optica* **2016**, *3*, 1504.
[186] W. Zhao, H. Jiang, B. Liu, J. Song, Y. Jiang, C. Tang, J. Li, *Sci. Rep.* **2016**, *6*, 30613.
[187] W. T. Chen, K.-Y. Yang, C.-M. Wang, Y.-W. Huang, G. Sun, I.-D. Chiang, C. Y. Liao, W.-L. Hsu, H. T. Lin, S. Sun, L. Zhou, A. Q. Liu, D. P. Tsai, *Nano Lett.* **2014**, *14*, 225.
[188] D. Wen, F. Yue, G. Li, G. Zheng, K. Chan, S. Chen, M. Chen, K. F. Li, P. W. H. Wong, K. W. Cheah, E. Y. B. Pun, S. Zhang, X. Chen, *Nat. Commun.* **2015**, *6*, 8241.
[189] L. Huang, H. Mühlenbernd, X. Li, X. Song, B. Bai, Y. Wang, T. Zentgraf, *Adv. Mater.* **2015**, *27*, 6444.
[190] M. Khorasaninejad, A. Ambrosio, P. Kanhaiya, F. Capasso, *Sci. Adv.* **2016**, *2*, e1501258.
[191] Z. Xie, T. Lei, G. Si, X. Wang, J. Lin, C. Min, X. Yuan, *ACS Photonics* **2017**, *4*, 2158.
[192] J. P. Balthasar Mueller, N. A. Rubin, R. C. Devlin, B. Groever, F. Capasso, *Phys. Rev. Lett.* **2017**, *118*, 113901.
[193] L. Huang, X. Chen, H. Mühlenbernd, H. Zhang, S. Chen, B. Bai, Q. Tan, G. Jin, K.-W. Cheah, C.-W. Qiu, J. Li, T. Zentgraf, S. Zhang, *Nat. Commun.* **2013**, *4*, 2808.
[194] Q. Wei, L. Huang, X. Li, J. Liu, Y. Wang, *Adv. Opt. Mater.* **2017**, *5*, 1700434.
[195] X. Zhang, J. Jin, M. Pu, X. Li, X. Ma, P. Gao, Z. Zhao, Y. Wang, C. Wang, X. Luo, *Nanoscale* **2017**, *9*, 1409.
[196] W. Ye, F. Zeuner, X. Li, B. Reineke, S. He, C.-W. Qiu, J. Liu, Y. Wang, S. Zhang, T. Zentgraf, *Nat. Commun.* **2016**, *7*, 11930.
[197] S. C. Malek, H.-S. Ee, R. Agarwal, *Nano Lett.* **2017**, *17*, 3641.
[198] L. Li, T. J. Cui, W. Ji, S. Liu, J. Ding, X. Wan, Y. B. Li, M. Jiang, C.-W. Qiu, S. Zhang, *Nat. Commun.* **2017**, *8*, 197.
[199] Y.-W. Huang, W. T. Chen, W.-Y. Tsai, P. C. Wu, C.-M. Wang, G. Sun, D. P. Tsai, *Nano Lett.* **2015**, *15*, 3122.
[200] B. Wang, F. Dong, Q.-T. Li, D. Yang, C. Sun, J. Chen, Z. Song, L. Xu, W. Chu, Y.-F. Xiao, Q. Gong, Y. Li, *Nano Lett.* **2016**, *16*, 5235.
[201] S. Choudhury, U. Guler, A. Shaltout, V. M. Shalaev, A. V. Kildishev, A. Boltasseva, *Adv. Opt. Mater.* **2017**, *5*, 1700196.
[202] W. Wan, J. Gao, X. Yang, *ACS Nano* **2016**, *10*, 10671.
[203] X. Li, L. Chen, Y. Li, X. Zhang, M. Pu, Z. Zhao, X. Ma, Y. Wang, M. Hong, X. Luo, *Sci. Adv.* **2016**, *2*, e1601102.
[204] X. Li, H. Ren, X. Chen, J. Liu, Q. Li, C. Li, G. Xue, J. Jia, L. Cao, A. Sahu, B. Hu, Y. Wang, G. Jin, M. Gu, *Nat. Commun.* **2015**, *6*, 6984.
[205] T. J. Cui, M. Q. Qi, X. Wan, J. Zhao, Q. Cheng, *Light: Sci. Appl.* **2014**, *3*, e218.
[206] L. H. Gao, Q. Cheng, J. Yang, S. J. Ma, J. Zhao, S. Liu, H. B. Chen, Q. He, W. X. Jiang, H. F. Ma, Q. Y. Wen, L. J. Liang, B. B. Jin, W. W. Liu, L. Zhou, J. Q. Yao, P. H. Wu, T. J. Cui, *Light: Sci. Appl.* **2015**, *4*, e324.
[207] L. J. Liang, M. Q. Qi, J. Yang, X. P. Shen, J. Q. Zhai, W. Z. Xu, B. B. Jin, W. W. Liu, Y. J. Feng, C. H. Zhang, H. Lu, H. T. Chen, L. Kang, W. W. Xu, J. Chen, T. J. Cui, P. H. Wu, S. G. Liu, *Adv. Opt. Mater.* **2015**, *3*, 1374.
[208] S. Liu, L. Zhang, Q. L. Yang, Q. Xu, Y. Yang, A. Noor, Q. Zhang, S. Iqbal, X. Wan, Z. Tian, W. X. Tang, Q. Cheng, J. G. Han, W. L. Zhang, T. J. Cui, *Adv. Opt. Mater.* **2016**, *4*, 1965.
[209] S. Liu, A. Noor, L. L. Du, L. Zhang, Q. Xu, K. Luan, T. Q. Wang, Z. Tian, W. X. Tang, J. G. Han, W. L. Zhang, X. Y. Zhou, Q. Cheng, T. J. Cui, *ACS Photonics* **2016**, *3*, 1968.
[210] S. Liu, T. J. Cui, Q. Xu, D. Bao, L. L. Du, X. Wan, C. M. Ouyang, H. Yuan, H. F. Ma, W. X. Jiang, J. G. Han, W. L. Zhang, Q. Cheng, *Light: Sci. Appl.* **2016**, *5*, e16076.
[211] B. Xie, K. Tang, H. Cheng, Z. Liu, S. Chen, J. Tian, *Adv. Mater.* **2016**, *29*, 1603507.
[212] B. Xie, H. Cheng, K. Tang, Z. Liu, S. Chen, J. Tian, *Phys. Rev. Appl.* **2017**, *7*, 024010.
[213] Y. B. Li, L. L. Li, B. B. Xu, W. Wu, R. Y. Wu, X. Wan, Q. Cheng, T. J. Cui, *Sci. Rep.* **2015**, *6*, 23731.
[214] D. Lao, L. Li, J. Ding, Y. B. Li, T. J. Cui, arXiv:1705.09387, **2017**.
[215] J. Li, P. Yu, H. Cheng, W. Liu, Z. Li, B. Xie, S. Chen, J. Tian, *Adv. Opt. Mater.* **2016**, *4*, 91.
[216] C. E. Shannon, *ACM SIGMOBILE Mobile Comput. Commun. Rev.* **2001**, *5*, 3.
[217] T. J. Cui, S. Liu, L. Li, *Light: Sci. Appl.* **2016**, *5*, e16172.
[218] S. Liu, T. J. Cui, L. Zhang, Q. Xu, Q. Wang, X. Wan, J. Q. Gu, W. X. Tang, M. Q. Qi, J. G. Han, W. L. Zhang, X. Y. Zhou, Q. Cheng, *Adv. Sci.* **2016**, *3*, 1600156.
[219] S. Liu, T. J. Cui, *IEEE J. Sel. Top. Quant.* **2017**, *23*, 1.
[220] S. Liu, T. J. Cui, *Sci. Rep.* **2016**, *6*, 37545.
[221] R. L. Haupt, *IEEE Trans. Antennas Propag.* **2005**, *53*, 2858.
[222] E. Maguid, I. Yulevich, D. Veksler, V. Kleiner, M. L. Brongersma, E. Hasman, *Science* **2016**, *352*, 1202.
[223] N. M. Litchinitser, *Science* **2016**, *352*, 1177.
[224] W. Liu, Z. Li, H. Cheng, S. Chen, J. Tian, *Phys. Rev. Appl.* **2017**, *8*, 014012.
[225] X. Chen, M. Chen, M. Q. Mehmood, D. Wen, F. Yue, C.-W. Qiu, S. Zhang, *Adv. Opt. Mater.* **2015**, *3*, 1201.

[226] M. Q. Mehmood, S. Mei, S. Hussain, K. Huang, S. Y. Siew, L. Zhang, T. Zhang, X. Ling, H. Liu, J. Teng, A. Danner, S. Zhang, C.-W. Qiu, *Adv. Mater.* **2016**, *28*, 2533.
[227] E. Arbabi, A. Arbabi, S. M. Kamali, Y. Horie, A. Faraon, *Sci. Rep.* **2016**, *6*, 32903.
[228] D. Veksler, E. Maguid, N. Shitrit, D. Ozeri, V. Kleiner, E. Hasman, *ACS Photonics* **2015**, *2*, 661.
[229] E. Maguid, I. Yulevich, M. Yannai, V. Kleniner, M. L. Brongersma, E. Hasman, *Light: Sci. Appl.* **2017**, *6*, e17027.
[230] C. Zhang, F. Yue, D. Wen, M. Chen, Z. Zhang, W. Wang, X. Chen, *ACS Photonics* **2017**, *4*, 1906.
[231] D. Wen, F. Yue, M. Ardron, X. Chen, *Sci. Rep.* **2016**, *6*, 27628.
[232] D. Wen, S. Chen, F. Yue, K. Chan, M. Chen, M. Ardron, K. F. Li, P. W. H. Wong, K. W. Cheah, E. Y. B. Pun, G. Li, S. Zhang, X. Chen, *Adv. Opt. Mater.* **2016**, *4*, 321.
[233] D. Lin, A. L. Holsteen, E. Maguid, G. Wetzstein, P. G. Kik, E. Hasman, M. L. Brongersma, *Nano Lett.* **2016**, *16*, 7671.
[234] X. Ma, M. Pu, X. Li, C. Huang, Y. Wang, W. Pan, B. Zhao, J. Cui, C. Wang, Z. Y. Zhao, X. Luo, *Sci. Rep.* **2015**, *5*, 10365.
[235] J. Jin, M. Pu, Y. Wang, X. Li, X. Ma, J. Luo, Z. Zhao, P. Gao, X. Luo, *Adv. Mater. Technol.* **2016**, *2*, 1600201.
[236] F. Yue, D. Wen, C. Zhang, B. D. Gerardot, W. Wang, S. Zhang, X. Chen, *Adv. Mater.* **2017**, *29*, 1603838.
[237] L. Huang, X. Song, B. Reineke, T. Li, X. Li, J. Liu, S. Zhang, Y. Wang, T. Zentgraf, *ACS Photonics* **2017**, *4*, 338.
[238] Y. Li, X. Li, L. Chen, M. Pu, J. Jin, M. Hong, X. Luo, *Adv. Opt. Mater.* **2016**, *5*, 1600502.
[239] D. Sell, J. Yang, S. Doshay, J. A. Fan, *Adv. Opt. Mater.* **2016**, *5*, 1700645.
[240] S. Boroviks, R. A. Deshpande, N. A. Mortensen, S. I. Bozhebolnyi, *ACS Photonics* **2017**, https://doi.org/10.1021/acsphotonics.7b01091.
[241] T. Cai, S. Tang, G. Wang, H. Xu, S. Sun, Q. He, L. Zhou, *Adv. Opt. Mater.* **2016**, *5*, 1600506.
[242] T. Cai, G. Wang, S. Tang, H. Xu, J. Duan, H. Guo, F. Guan, S. Sun, Q. He, L. Zhou, *Phys. Rev. Appl.* **2017**, *8*, 034033.
[243] D. Ohana, B. Desiatov, N. Mazurski, U. Levy, *Nano Lett.* **2016**, *16*, 7956.
[244] D. Ohana, U. Levy, *Opt. Express* **2014**, *22*, 27617.
[245] A. Y. Piggott, J. Lu, K. G. Lagoudakis, J. Petykiewicz, T. M. Babinec, J. Vučković, *Nat. Photonics* **2015**, *9*, 374.
[246] B. Shen, P. Wang, R. Polson, R. Menon, *Nat. Photonics* **2015**, *9*, 378.
[247] Y. Xu, C. Gu, B. Hou, Y. Lai, J. Li, H. Y. Chen, *Nat. Commun.* **2013**, *4*, 2561.
[248] H. Wang, Y. Xu, P. Genevet, J.-H. Jiang, H. Y. Chen, *Sci. Rep.* **2016**, *6*, 24529.
[249] C. Gong, J. Zhang, S. He, *Opt. Lett.* **2017**, *42*, 5098.
[250] A. Pors, S. I. Bozhevolnyi, *Phys. Rev. Appl.* **2016**, *5*, 064015.
[251] T. Amemiya, T. Kanazawa, S. Yamasaki, S. Arai, *Materials* **2017**, *10*, 1037.
[252] Z. Li, M.-H. Kim, C. Wang, Z. Han, S. Shrestha, A. C. Overvig, M. Lu, A. Stein, A. M. Agarwal, M. Lončar, N. Yu, *Nat. Nanotechnol.* **2017**, *12*, 675.
[253] C. Wang, Z. Li, M.-H. Kim, X. Xiong, X.-F. Ren, G.-C. Guo, N. Yu, M. Lončar, *Nat. Commun.* **2017**, *8*, 2098.
[254] M. Principe, M. Consales, A. Micco, A. Crescitelli, G. Castaldi, E. Esposito, V. L. Ferrara, A. Cutolo, V. Galdi, A. Cusano, *Light Sci. Appl.* **2017**, *6*, e16226.
[255] A. M. Shaltout, A. V. Kildishev, V. M. Shalaev, *J. Opt. Soc. Am. B* **2016**, *33*, 501.
[256] A. Komar, Z. Fang, J. Bohn, J. Sautter, M. Decker, A. Miroshnichenko, T. Pertsch, I. Brener, Y. S. Kivshar, I. Staude, D. N. Neshev, *Appl. Phys. Lett.* **2017**, *110*, 071109.
[257] J. Park, J.-H. Kang, S. J. Kim, X. Liu, M. L. Brongersma, *Nano Lett.* **2017**, *17*, 407.
[258] Z. Liu, S. Chen, H. Cheng, Z. Li, W. Liu, J. Tian, *Plasmonics* **2016**, *11*, 353.
[259] Z. Liu, S. Chen, J. Li, H. Cheng, Z. Li, W. Liu, P. Yu, J. Xia, J. Tian, *Opt. Lett.* **2014**, *39*, 6763.
[260] Y. Chen, X. Li, Y. Sonnefraud, A. I. Fernández-Domínguez, X. Luo, M. Hong, S. A. Maier, *Sci. Rep.* **2015**, *5*, 8660.
[261] J. Sautter, I. Staude, M. Decker, E. Rusak, D. N. Neshev, I. Brener, Y. Kivshar, *ACS Nano* **2015**, *9*, 4308.
[262] J. Y. Ou, E. Plum, L. Jiang, N. I. Zheludev, *Nano Lett.* **2011**, *11*, 2142.
[263] L. Zou, M. Cryan, M. Klemm, *Opt. Express* **2014**, *22*, 24142.
[264] C. H. Chu, M. L. Tseng, J. Chen, P. C. Wu, Y.-H. Chen, H.-C. Wang, T.-Y. Chen, W. T. Hsieh, H. J. Wu, G. Sun, D. P. Tsai, *Laser Photonics Rev.* **2016**, *10*, 986.
[265] K. Chen, Y. Feng, F. Monticone, J. Zhao, B. Zhu, T. Jiang, L. Zhang, Y. Kim, X. Ding, S. Zhang, A. Alù, C.-W. Qiu, *Adv. Mater.* **2017**, *29*, 1606422.
[266] A. Shaltout, A. Kildishev, V. Shalaev, *Opt. Mater. Exp.* **2015**, *5*, 2459.
[267] Y. Hadad, D. L. Sounas, A. Alù, *Phys. Rev. B* **2015**, *92*, 100304.
[268] F. Walter, G. Lin, C. Meier, S. Zhang, T. Zentgraf, *Nano Lett.* **2017**, *17*, 3171.
[269] J. Lee, M. Tymchenko, C. Argyropoulos, P.-Y. Chen, F. Lu, F. Demmerle, G. Boehm, M.-C. Amann, A. Alù, M. A. Belkin, *Nature* **2014**, *511*, 65.
[270] N. Segal, S. Keren-Zur, N. Hendler, T. Ellenbogen, *Nat. Photonics* **2015**, *9*, 180.
[271] M. Asano, M. Bechu, M. Tame, Ş. K. Özdemir, R. Ikuta, D. Ö. Güney, T. Yamamoto, L. Yang, M. Wegener, N. Imoto, *Sci. Rep.* **2015**, *5*, 18313.
[272] P. K. Jha, X. Ni, C. Wu, Y. Wang, X. Zhang, *Phys. Rev. Lett.* **2015**, *115*, 025501.
[273] P. K. Jha, N. Shitrit, J. Kim, X. Ren, Y. Wang, X. Zhang, *ACS Photonics* **2018**, *5*, 971.